quaternary

MDPI

Article

Formation and Cyclicity Patterns of Dust-Enriched Quaternary Sediment Archives on the Eastern Canary Islands

Jakob Labahn [1,*], Dominik Faust [1], Thomas Kolb [2], Anja Maria Schleicher [3], Christina Günter [4], Carsten Marburg [1] and Christopher-Bastian Roettig [1]

[1] Department of Geography, Dresden University of Technology, 01069 Dresden, Germany; dominik.faust@tu-dresden.de (D.F.); carsten.marburg@tu-dresden.de (C.M.); christopher-bastian.roettig@tu-dresden.de (C.-B.R.)
[2] Institute of Geography, Justus-Liebig-University, 35390 Gießen, Germany; thomas.r.kolb@geogr.uni-giessen.de
[3] GFZ Helmholtz Centre for Geosciences, 14473 Potsdam, Germany; anja.maria.schleicher@gfz.de
[4] Institute of Geosciences, University of Potsdam, 14476 Potsdam-Golm, Germany; christina.guenter@geo.uni-potsdam.de
* Correspondence: jakob.labahn@tu-dresden.de

Abstract

By its availability and deposition dust is a key indicator for past climate variability. Due to the location in the main North African dust corridor, the Canary Islands preserve dust deposits in different geoarchives—for instance in valleys dammed by Quaternary volcanism. These basins act as sediment traps for aeolian, volcanic, and slope-derived material, forming alternating pale, carbonate-enriched (PCLs) and reddish, clay-enriched layers (RCLs). However, the extent to which these sequences retain primary dust signals remains uncertain. We examine the interpretability of locally called vega sediments by disentangling input pathways, post-depositional processes, and geomorphological controls. Two sections on Lanzarote (Teguise, Femés) and the section Vallebrón (Fuerteventura) were investigated using grain-size analysis, XRF and XRD measurements, and IRSL dating. The sequences reveal two dust components: high-intensity dust fall events forming PCLs, and persistent finer dust input preserved in RCLs through kaolinite. Many PCLs originated as loess-like deposits subsequently modified by carbonate redistribution, while clay mineral transformations complicate provenance interpretation. Archive clarity varies with geomorphology, from less distinctly layered, patchy carbonate-enriched succession at Vallebrón to continuous cyclic sequences in Teguise. Overall, these basins preserve both episodic dust events and continuous fine-grained input, offering a valuable framework for reconstructing Late Quaternary dust dynamics.

Keywords: environmental reconstruction; aeolian sediment; palaeosols; calcretes; secondary carbonates; clay minerals; arid landscapes; basin; Canary Islands

Academic Editor: Yan Li

Received: 17 November 2025
Revised: 16 January 2026
Accepted: 26 January 2026
Published: 4 February 2026

1. Introduction

Mineral dust is a key driver of environmental and climatic processes as its long-range transport affects atmospheric chemistry [1], ocean fertilisation [2], and terrestrial ecosystems [3–7]. In addition, it serves as a valuable proxy for reconstructing palaeoclimatic dynamics [8–11]. Dust is predominantly emitted from arid and semi-arid regions, forming the "dust belt" that stretches from North Africa across the Middle East to Central and East Asia [9,12]. Among these regions, North Africa is by far the most important modern dust source, encompassing potential source areas (PSAs) ranging from the hyper-arid Sahara

to the semi-arid Sahel [13]. Dust emissions from these areas are transported across the Atlantic and beyond, with large fluxes carried westward by the trade winds, the Saharan Air Layer, and other circulation systems [14]. The Canary Islands—especially Lanzarote and Fuerteventura due to their close position to the African continent—are located directly within this transport corridor and are therefore ideally situated to archive long-term dust inputs.

Among the most promising terrestrial archives in this region are trapped sediments in locally so-called "vegas". These "vegas" are valleys that were dammed by volcanic activity during the Quaternary, forming closed sedimentary basins that trapped aeolian dust, volcanic particles, and colluvial slope material [15]. Their stratigraphy typically consists of pale, carbonate-enriched layers (PCLs) alternating with reddish, clay-enriched layers (RCLs)—whereby 'clay-enriched' refers to the dominance of the clay-sized fraction rather than an enrichment in specific clay minerals. This alternation reflects cyclic deposition patterns. In a series of studies [16–18], von Suchodoletz et al. discussed that these alternations are linked to orbital-scale variations resulting in varying soil moisture and dust supply. A distinct loess-like layer preserved in the vega sections of Teguise and Femés has been interpreted as the record of a short-lived dust event caused by intense land use [19]. Based on geomorphological analyses and luminescence dating presented in these studies, a robust chronostratigraphic framework was established, dating back to ~180 ka. These studies also showed that vegas function as effective sediment traps, recording both aeolian inputs and pedogenic processes, resulting in stratigraphies that archive variations in dust supply and environmental conditions over time. To disentangle the interpretability of dust deposits within vega archives, we need to investigate the processes controlling the formation of vega sections. Therefore, we examine two previously studied sites on Lanzarote (Teguise and Femés) and include a new section from a non-dammed but drained system, the Vallebrón catchment on Fuerteventura. This shall allow us to distinguish between sediment characteristics associated with a damming situation and those that are ubiquitously distributed. The study addresses the following main research question:

How do vega sequences form, what information do they preserve over long timescales, and to what extent can their dust signals be interpreted? This overarching question is explored through the following sub-questions:

- What materials are involved in the formation of vega sequences?
    - What sediments reach the vega systems, and what sediment characteristics are linked to pre-sedimentary processes?
    - How do sediments enter the vega archives?
- What post-sedimentary processes take place?
- What characteristics are linked to the damming situation of the vega systems, and which influences and processes are not attributed to that specific situation?

2. Materials and Methods

2.1. Geographical Setting and State of Research

The Canary Islands form a volcanic archipelago in the subtropical Atlantic, located off the northwestern African coast (see Figure 1). For most of the year, the islands are influenced by the northeastern trade winds. Due to the higher altitudes, the western islands receive more precipitation, while the eastern islands—Lanzarote and Fuerteventura—receive little to no orographic precipitation. The highest elevations are Pico de la Zarza (807 m.a.s.l.) on Fuerteventura and Peñas del Chache (672 m.a.s.l.) on Lanzarote. The cold Canary Current further moderates temperatures and suppresses rainfall, resulting in a dry, semi-arid to arid climate on the Eastern Canary Islands, with annual precipitation varying from

~100 mm in lowland areas to ~250 mm at higher altitudes. Respectively, the vegetation cover on Lanzarote and Fuerteventura is sparse and predominantly consists of xerophytic and halophytic species [17]. Plant communities are adapted to water scarcity and high evaporation rates [17].

The eastern Canary Islands reflect multiple phases of volcanic activity. On Lanzarote, volcanism began in the Miocene (~15.5 Ma) and continued until historical times with the last eruption in 1824 [20]. The island is structured into two volcanic massifs of Miocene to Pliocene age, the Guatifay-Famara massif in the north and the Los Ajaches massif in the south (see Figure 1) [21]. Younger Pleistocene and Holocene lava fields and pyroclastics dominate the centre and southwest (Montañas del Fuego). Aeolian sand sheets and palaeodunes are preserved near Mala and southwest of Famara. Fuerteventura shares a similar volcanic history but also exposes older units such as the Cretaceous "Basal Complex," which is visible in the island's central and northwestern parts [22]. Aeolian deposits on both islands are largely of Pleistocene and Holocene origin.

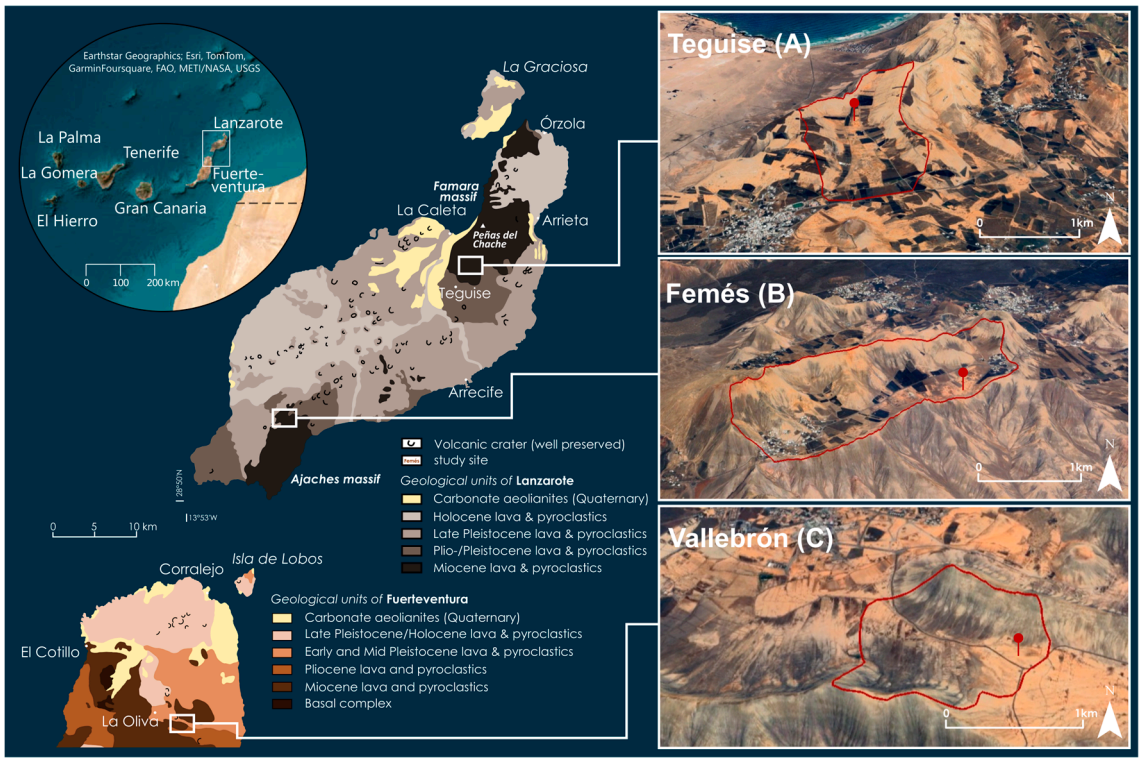

Figure 1. Geological setting and catchments of the investigated sites. Geological overview of Lanzarote and northern Fuerteventura showing major volcanic units (modified after [21]) and the location of the study sites. The inset map (**top left**) illustrates the position of the eastern Canary Islands off the northwest African coast (ArcGIS Pro 2.8.0). Panels (**A**–**C**) show the catchments of Teguise (**A**) and Femés (**B**) on Lanzarote—both located in valleys dammed by Quaternary volcanism—and the undammed catchment of Vallebrón (**C**) on Fuerteventura. Catchment boundaries are delineated with red lines; red pins indicate the position of the investigated sections (maps modified from Google Earth imagery).

The landscape of both islands reflects long-term erosional processes, which have smoothed the volcanic relief into broad concave slopes dissected by gullies and covered by extensive alluvial fans [23]. In the eastern islands, prolonged hyper-arid conditions and seismic stability appear to have strongly limited erosion, allowing the preservation of relict surfaces such as polygenetic calcretes that formed during successive phases of soil development [17]. During the Early to Middle Pleistocene, volcanic damming in several valleys created the vega systems that today act as natural sediment traps.

Within these closed basins, material from various sources accumulated, including volcanic bedrock, colluvial slope sediments, and aeolian dust transported from potential source areas across North Africa. Dust reaches the eastern Canary Islands via several wind systems: (1) north-easterly trade winds carry dust at low altitudes throughout the year; (2) the Saharan Air Layer (SAL) transports material from the southern Sahara and Sahel at altitudes of 5–7 km, particularly in summer; and (3) the Harmattan conveys dust westward in winter toward the coastal fringe of West Africa [24]. In addition, the region regularly experiences 'Calima' episodes—a local meteorological phenomenon known for transporting warm, dust-laden air from the Sahara that forms a hazy, low-visibility layer over the islands [25]. These dusty outbreaks significantly affect local atmospheric conditions. The deposited aeolian material is predominantly silty and contains substantial proportions of carbonates (up to 40%), feldspars, quartz, and clay minerals—particularly illite, kaolinite, montmorillonite, and palygorskite [13,17,25–27]. Since quartz is largely absent in the volcanic geology of Lanzarote and only occurs in the "Basal Complex" on Fuerteventura, it is widely used as a tracer for dust input [24,28–30]. The recurring alternation of PCLs and RCLs has been interpreted as reflecting loess-like aeolian deposits and more pedogenically overprinted units, respectively [15–18]. This cyclicity is thought to result from orbital-scale shifts in soil moisture linked to changes in Earth's obliquity, which regulated dust availability and pedogenic intensity. These dynamics are recorded in the vega sequences over at least the past 180,000 years, underlining their potential as long-term terrestrial dust archives.

2.2. Study Sites

The Teguise vega section (29°04′08″ N, 13°30′55″ W) is situated in a north–south oriented valley at the southern margin of the Famara Massif in northern Lanzarote. The catchment covers approximately 3.8 km^2, of which about 35% corresponds to the valley floor, resulting in a low slope-to-valley ratio of 2.9:1 [15]. Volcanic damming in the southern part of the valley occurred during the Early Pleistocene, around 1.2 Ma ago, but remains incomplete. The surrounding slopes are gently inclined, rising up to 100 m above the valley floor, and are partly dissected by gully erosion. The valley floor sediments in the northern sector exhibit horizontal stratification with alternating yellowish, silty PCLs and RCLs, often intersected by carbonate veins and cracks (see Figure 2A). These layers fade out upslope, forming laterally continuous deposits. In contrast, the southern part of the valley reveals an erosional gap and disturbed stratigraphy, likely caused by sediment discharge due to the incomplete damming.

The vega of Femés (28°55′32″ N, 13°45′19″ W) is located in the Los Ajaches Massif in southern Lanzarote. It extends over a length of approximately 3 km from SW to NE and encompasses a catchment area of 5.07 km^2. The valley floor covers about 18.4% of the total area, yielding a slope-to-valley ratio of 5.4:1 [15]. Volcanic damming occurred around 1 Ma ago and is considered complete. Compared to Teguise, the slopes are significantly steeper, rising up to 200 m above the valley floor. The sediments consist of horizontally bedded sequences of RCLs interbedded with lighter, silty PCLs. These sequences often show internal differentiation, such as sub-layers and lateral variations (see Figure 2B). Despite the steeper relief, individual beds can be traced laterally upslope before thinning out. The transition zone between slopes and the valley floor is frequently marked by small alluvial fans.

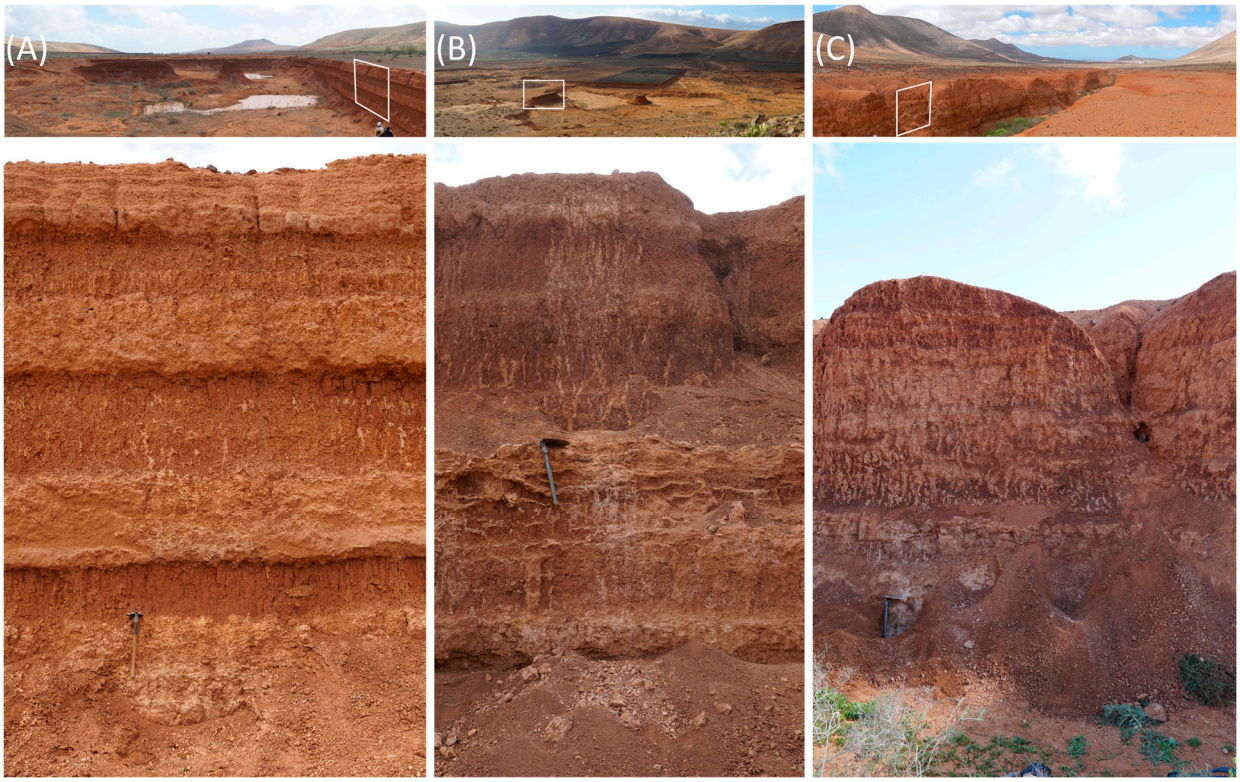

Figure 2. Overview of the three investigated study sites. White rectangles show the position of the sections, with their respective photos below. (**A**) Vega Teguise (Lanzarote) with a pronounced alternation of (lighter) PCLs and (darker) RCLs; (**B**) Vega Femés (Lanzarote), showing a valley with steeper slopes and a more complex stratigraphy; (**C**) Vallebrón (Fuerteventura), an undammed catchment with reduced layer thicknesses and less pronounced layering.

The Vallebrón site (28°35′44.6″ N, 13°54′25.3″ W) is located in a small valley in northern Fuerteventura, southeast of La Oliva. The valley extends over approximately 2 km^2 in an east–west orientation and lies between two mountain ridges. The site is positioned near the watershed at the upper valley section, just 100 m from the divide to the neighbouring catchment. Unlike the dammed vegas on Lanzarote, Vallebrón has not been blocked by volcanic activity and thus represents an open sedimentary system. Sediments are exposed up to 5 m deep and exhibit an alternation of patchy, carbonate-bearing layers and reddish, carbonate-free clay bands (see Figure 2C). Downstream, sediment thickness declines rapidly, and stratigraphic layering becomes less distinct—suggesting episodic sedimentation and partial erosion.

2.3. Fieldwork

We collected sediment samples from the three sites of Teguise, Femés, and Vallebrón for XRD and XRF measurements, OSL dating, and grain-size analyses. In Teguise and Femés, equidistant sampling was carried out at 10 cm intervals. At Vallebrón, the porous structure of the sediment deposits prevented systematic interval sampling; instead, samples were taken by stratigraphic units, targeting the transitions between identified sediment layers. In addition, a higher-resolution sampling of carbonate-filled cracks and clay-rich material was conducted to characterise post-depositional features in greater detail. All sections were described with regard to the sedimentological composition of the parent material, hydromorphic features, evidence of relocation, and indicators of aeolian input.

2.4. Grain-Size Distribution and $CaCO_3$ Content

The particle size distributions were measured with a Horiba LA950v2 laser diffraction particle sizer at GFZ Helmholtz Centre for Geosciences (Potsdam, Germany). The air-dried samples were suspended in 2.5 mL of sodium pyrophosphate for 24 h, and neither calcium carbonate nor organic material was removed. Each sample was measured 10 times consecutively using ultrasound. Due to occasionally reduced laser transmittance during measurement, multi-scattering effects may have led to an overestimation of particles in the <1 µm fraction. The values shown are the medians of 82 classes between 0.044 and 2500 µm. Grain-size plots were created with the software RStudio 2024.04.02. The grain-size distributions were plotted as heatmaps [31] representing the percentage of each class. The heatmaps are divided into three matrices (see below in the grain-size figures, e.g. in Section 3.1). The first matrix represents the clay fraction and ranges from 0.044 to 1.981 µm. The second matrix represents the silt fraction and ranges from 1.981 to 58.953 µm. The third matrix contains the grain-sizes from 58.953 to 2500 µm and represents the sand fraction. The cumulative percentage of the three matrices (per sample) is shown at the top of the grain-size figures and illustrated by bar charts (see below, e.g. in Section 3.1).

The $CaCO_3$ content was determined by treating the samples with hydrochloric acid and measuring in a Scheibler apparatus [32] at the Geographical Laboratory of the Dresden University of Technology (Dresden, Germany).

2.5. XRD Analysis

As part of the preparation, the air-dried samples were sieved to a grain size of <63 µm. XRD measurements were carried out at the University of Potsdam (Potsdam, Germany) with a sample rotation at 1 s-1 using a PANalytical Empyrean powder X-ray diffractometer (Bragg–Brentano geometry). The diffractometer was equipped with a PIXcel1D detector and operated with Cu Kα radiation (λ = 1.5419 Å) at 40 kV and 40 mA. The range of scan varied from 4 to 70°2θ (overview scan) to 2 to 34°2θ (glycolated and heated clay mineral samples). The reflexes selected for measurement for the respective minerals were 8.6°2θ (±0.1°2θ) for illite, 12.3°2θ (±0.1°2θ) for kaolinite, and 26.6°2θ (±0.05°2θ) for quartz. Peak evaluation was conducted using HighScore Plus 4.0 software, and results obtained by profile fitting are expressed as relative values normalised to the background.

2.6. XRF Analysis

To determine the elemental composition, the air-dried samples were ground twice and subsequently passed through a 63 µm sieve. The elemental composition of the mineral powder was analysed using fused beads with an AXIOS Advanced XRF Spectrometer (MalvernPANalytical) at the ElMiE Lab—GFZ Helmholtz Centre for Geosciences. Elements (Fe, K, Mn, Sr, Zn, Zr) were determined with a quantification level (QL) of 0.02 wt% for the wt% range and 10 ppm for mg/kg. Zn, Sr, and Zr were measured in mg/kg, whereas Fe_2O_3, MnO, and K_2O were determined in wt% and therefore reported as oxides. For simplicity, these oxide values are referred to as the respective elements (Fe, Mn, K) throughout the article, except in the section figures in Sections 3.1–3.3.

2.7. Luminescence Dating

A total of 22 luminescence samples from the polymineral fine-grain fraction (4–11 µm) were analysed to establish local chronologies for the investigated sites. Sampling was conducted at night using opaque plastic bags to prevent light exposure. Sample preparation followed standard procedures [33] under subdued amber-light conditions. After wet sieving into defined grain-size fractions (<38 µm, 38–63 µm, 63–90 µm, and 90–200 µm), carbonates and organic matter were removed using 10% HCl and 10% H_2O_2, respectively.

During treatment of the <38 µm fraction, pH was continuously monitored to prevent flocculation at values below 3. The polymineral fine-grain fraction (4–11 µm) was then isolated from the <38 µm material by gravitational settling in Atterberg cylinders, applying settling times based on Stokes' law.

Luminescence measurements were carried out at Justus Liebig University Giessen using automated Freiberg Instruments Lexsyg Smart and Lexsyg Research readers equipped with internal $^{90}Y/^{90}Sr$ β-sources and infrared LEDs (850 nm, 150 mW/cm^2). The emitted signal was detected using a Hamamatsu H7360 photomultiplier tube after passing through a filter combination of an AHF Brightline HC414/46 and a Schott BG39, centering detection at approximately 410 nm.

A modified single-aliquot regenerative-dose (SAR) protocol was applied following [34,35]. IRSL signals were recorded for 300 s at an elevated temperature of 125 °C after a 20 min pause following the preheat step. Equivalent doses (De) were derived from single saturating exponential fits to the dose–response curves, using the first 5 s of the IRSL signal after subtraction of a background obtained from the last 50 s. Only aliquots with recycling ratios between 0.9 and 1.1, recuperation $\leq$5% of the natural sensitivity-corrected signal [36,37], and signal intensities at least three times the background were accepted. Final equivalent dose estimates were obtained using the Central Age Model (CAM) [38].

To assess potential signal instability, fading tests were performed on selected samples, revealing generally low fading rates of 1–2.5% per decade. In addition, bleaching experiments were conducted to determine residual doses, which were consistently very low and typically below 1% of the corresponding palaeodose. Consequently, neither fading corrections nor residual-dose corrections were applied.

Radionuclide concentrations were determined using a combined alpha- and beta-counting approach with the µDose system [39,40]. To account for small-scale variability in the gamma dose rate, bulk dose-rate samples were collected within a 30 cm radius around each OSL sampling point. Water contents of 15 $\pm$ 5% were applied, based on present-day moisture measurements and adjusted for site-specific sedimentological and geomorphological conditions. Cosmic dose rates were calculated following [41] using the 'calc_CosmicDoseRate' function of the R package Luminescence [42].

Data processing was performed using modified routines of the R package Luminescence [42]. Dose rates and final age estimates were obtained with the Dose Rate and Age Calculator (DRAC v1.2 [43], applying the conversion factors proposed by [44].

2.8. Figures

The section figures were created using Inkscape software version 1.0. Bar plots of elemental and mineralogical composition, as well as heatmap images of grain-size distributions, were generated with RStudio 2024.04.02 and subsequently transferred to Inkscape. The height of each bar corresponds to the relative value of the respective sample.

3. Results

3.1. Teguise Section

3.1.1. Stratigraphy and Sedimentary Architecture

The section of Teguise (see Figure 3) comprises 14 distinct sediment layers (SLs), which are grouped into three vega sequences (VS 1–3) based on their stratigraphic arrangement and compositional characteristics.

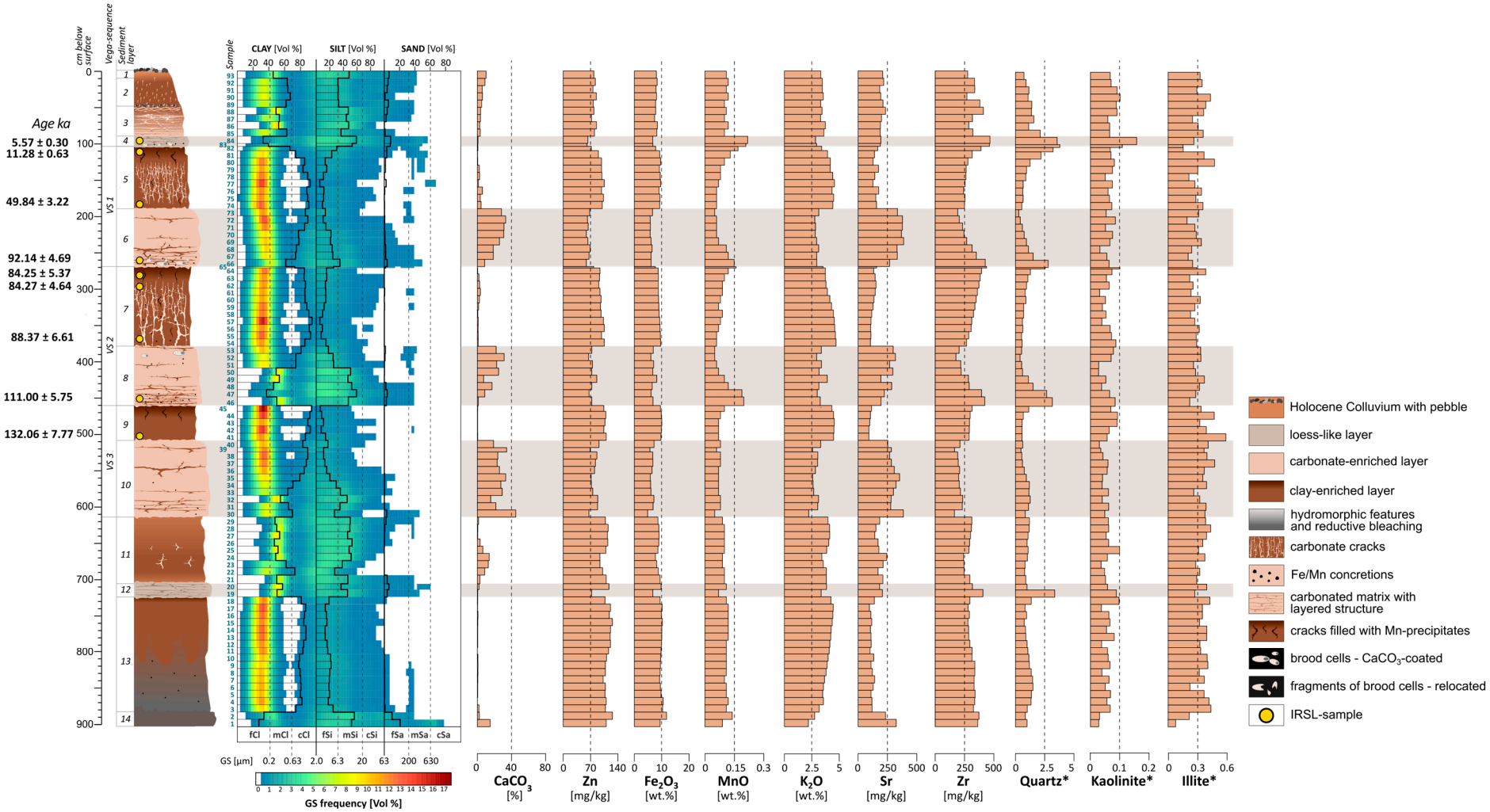

Figure 3. Section of Teguise with analytical data of the samples. Grain-size distributions are shown as heatmaps (frequency of a class in % Vol). Black lines show the cumulative percentage of clay, silt, and sand. * Minerals are normalised to the sample-specific background and represent relative peak intensities.

Each sequence consists of a pair of reddish clay-enriched layers (RCLs) and pale carbonate-enriched layers (PCLs). Two additional loess-like layers (SL 4 and SL 12) are intercalated as individual units. The lowermost part of the section (SL 11, SL 13, SL 14) deviates from this alternating pattern. SL 11 appears as a transitional, clayey-silty layer that cannot be clearly classified as either a PCL or an RCL. SL 13 and SL 14 are also compositionally distinct and exhibited clear redoximorphic features in the field. A detailed description of all sediment layers is provided in Appendix A.1, Table A1. The section is located in the upper valley, where the catchment area is approximately 1.1 km^2. In this section, the stratigraphy exhibits a well-developed horizontal layering with alternating PCLs and RCLs, each with a thickness between 50 and 100 cm. This regular layering is continuous across the valley floor. On adjacent slopes, sediment layers fade out progressively with elevation, and PCLs exposed at the surface are transformed into hardened calcareous crusts.

In the lower, southern part of the valley, where the catchment area expands to 3.8 km^2, the uppermost sediments are dominated by gravel and stone fragments deposited in discontinuous bands. While horizontally layered strata occur below these gravels, no correlation with the sequence observed in the upper valley could be established so far.

3.1.2. Reddish Clay-Enriched Layers (RCLs)

The RCLs (SL 5, SL 7, SL 9) are characterised by a dense, $CaCO_3$-poor matrix and contain the highest clay contents in the section, reaching up to 94.7% (SL 7, sample 57). The grain-size distribution is dominated by the clay fraction. In SL 5 and SL 7, the upper parts contain more silt, which decreases with depth, while clay content increases. Vertical fissures filled with Mn precipitates occur in the upper parts and diminish downward, in parallel with decreasing Mn concentrations. The geochemical and mineralogical signatures of the RCLs show strong similarities. Quartz, Zr, and TiO_2 values decrease with depth, while Zn and Fe remain high and relatively constant. Below the top 10–20 cm, vertical carbonate-filled fissures become increasingly common, except in SL 9, where they are absent.

3.1.3. Pale Carbonate-Enriched Layers (PCLs)

The PCLs (SL 6, SL 8, SL 10) exhibit maximum carbonate concentrations of 45.0% (SL 10), 33.2% (SL 6), and 31.4% (SL 8). In SL 6 and SL 8, $CaCO_3$ contents are higher in the upper parts and decrease downward; in SL 10, the highest carbonate content is found at the base. Clay content remains high (up to 90%) in the upper sections, dominated by fine particles (<0.2 μm). In the lower parts of the layers, clay content decreases while silt increases (e.g., 60% in SL 8, sample 47), accompanied by rising concentrations of quartz, Zr, and Mn. Mn concretions and Mn-coated insect nests are frequently observed at the base, along with compact, horizontally stratified calcareous bands. Sr values are elevated throughout the PCLs, especially in the upper segments.

3.1.4. Loess-like Layers

SL 4 and SL 12 are thin (10–20 cm) and silt-rich, with silt contents of 60% and 45%, respectively. These layers feature the highest quartz and Zr concentrations in the section and elevated kaolinite contents. SL 4 also contains Fe-Mn concretions and manganese-filled brood cells.

3.2. Femés Section

3.2.1. Stratigraphy and Sedimentary Architecture

The section of Femés (see Figure 4) comprises 11 sediment layers (SLs), grouped into three main vega sequences consisting of alternating RCLs and PCLs, along with an additional upper loess-like layer (SL 2) and several intermediate clayey-silty units. A detailed description of all sediment layers is provided in Appendix A.1, Table A2.

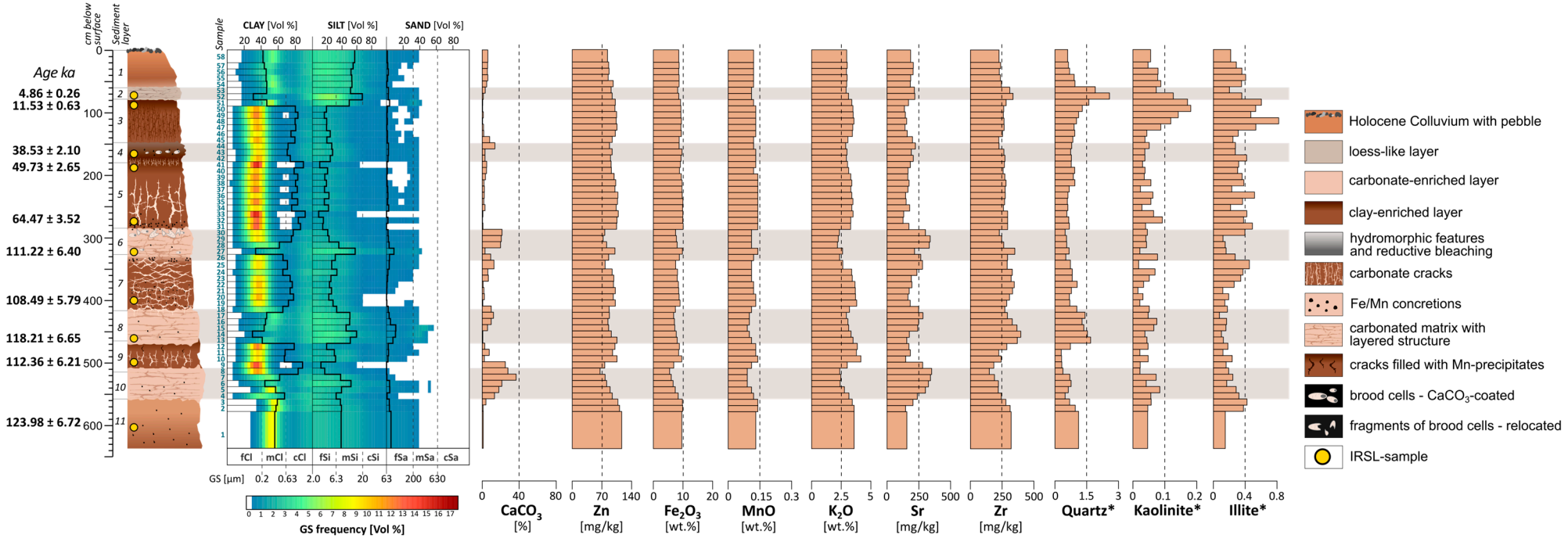

Figure 4. Section of Femés with analytical data of the samples. Grain-size distributions are shown as heatmaps (frequency of a class in % Vol). Black lines show the cumulative percentage of clay, silt, and sand. * Minerals are normalised to the sample-specific background and represent relative peak intensities.

The section is situated within a dammed valley in the Los Ajaches Massif, with a total catchment area of 5.07 km^2. The immediate valley floor at the outcrop is relatively broad, but the surrounding slopes are steeper than in Teguise and rise up to 200 m above the valley floor. The vega sequences at this site exhibit horizontal layering, although subtle sub-layering and lateral convergence of layers can be observed within the closer surroundings of the section. Layer thickness ranges between 40–100 cm for RCLs and 50–60 cm for PCLs. On adjacent slopes, the layers fade out upward, and PCLs transition into surface calcareous crusts.

3.2.2. Reddish Clay-Enriched Layers (RCLs)

The RCLs (SL 3, SL 5, SL 7, SL 9) are characterised by a fine-textured, carbonate-poor matrix with clay contents of up to 92% (SL 5, sample 33). Clay dominates the grain-size distributions. Silt content varies across layers, with no consistent vertical trend. Mn precipitates are common in SL 3, SL 5, and SL 7, occurring as bands, coatings, or embedded within clay aggregates. The Mn content remains relatively constant with depth. Vertical and horizontal carbonate-filled fissures are present in all RCLs, but their development varies. SL 5 contains the most prominent vertical cracks (up to 80 cm), while SL 7 shows a combination of horizontal and vertical fissures forming a lattice-like pattern. SL 3 exhibits minimal carbonate fissuring. In terms of geochemistry, quartz concentrations decrease downward in SL 3, while Ti and Zr remain stable in most layers. Overall, RCLs show elevated and stable Zn and Fe values.

3.2.3. Pale Carbonate-Enriched Layers (PCLs)

PCLs in Femés (SL 6, SL 8, SL 10) exhibit carbonate concentrations of up to 36.5% (SL 10). Carbonate contents are typically higher in the upper segments of the layers. Clay contents reach a maximum of 83.2% (SL 10, sample 8). Toward the base, clay fractions decrease while silt increases, reflected in grain-size distributions and higher quartz and Zr values. Quartz peaks are especially pronounced at the base of SL 8, accompanied by Zr maxima. Zr values also increase downwards in SL 6 and SL 10. Mn concretions are present throughout the PCLs, and SL 6 contains abundant calcified brood cells. Sr concentrations increase upwards within the layers and are consistently elevated.

3.2.4. Loess-like Layer

The loess-like layer (SL 2) is located near the top of the section and is 10–20 cm thick with a silt content of 51%. It contains the highest quartz and Zr concentrations in the section and elevated kaolinite values. Mn levels are also increased, while carbonate content remains low (<3.2%). Figure 5 illustrates the stratigraphy of the Femés section and the spatial properties of the individual sediment layers. The illustration shows slight sub-layering and local variations in bedding geometry, including dipping and converging layers. It also depicts the distribution of carbonate features, such as vertical and horizontal fissures, patchy precipitation zones, and carbonate coatings.

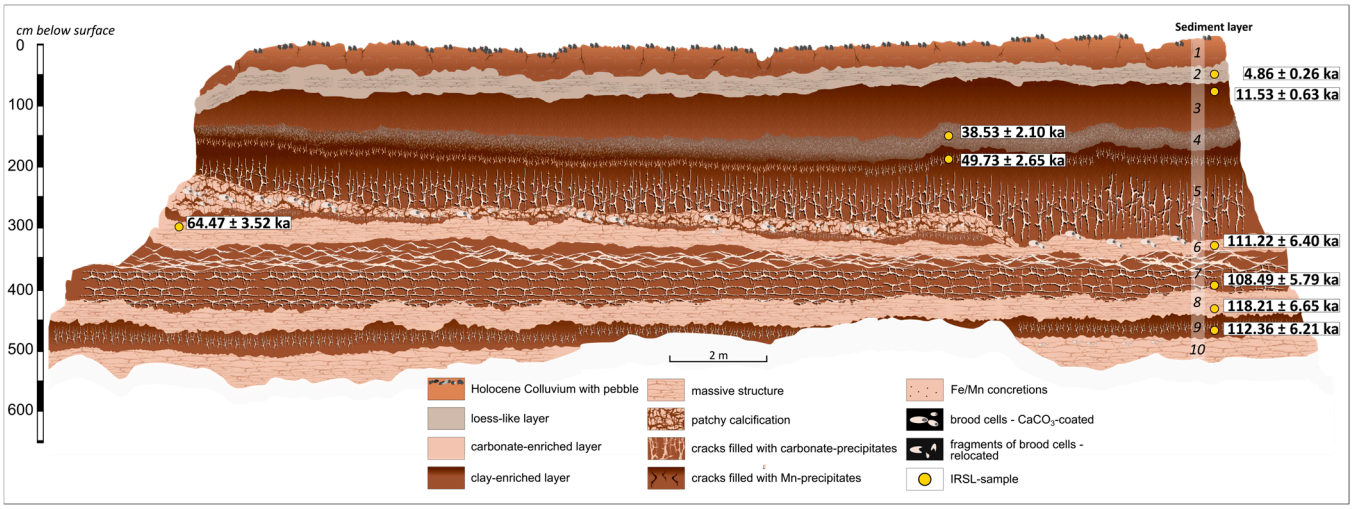

Figure 5. Femés section showing sediment layers, carbonate features, and positions of IRSL samples.

3.3. Vallebrón

3.3.1. Stratigraphy and Sedimentary Architecture

The Vallebrón section (see Figure 6) comprises 12 sediment layers (SLs) located within an undammed valley in northern Fuerteventura. The site is positioned in the upper catchment, near the watershed, with a contributing area of approximately 2 km^2. A detailed description of all sediment layers is provided in Appendix A.1, Table A2.

The stratigraphy is characterised by a horizontally layered alternation between five thin but well-defined clay-enriched layers (SL 3, 5, 7, 9, 11) and four patchy, carbonate-enriched layers (SL 2, 4, 6, 8), in addition to two more consolidated PCLs (SL 10 and SL 12) at the base and top of the section. The clay-enriched layers range in thickness from 10–20 cm, while the carbonate-enriched layers vary between 40–90 cm. Particularly in the lower part of the section, between SL 10 and SL 12, the alternation of clay- and carbonate-dominated deposits is well preserved. Laterally, slight shifts and variations in layer continuity occur, especially between the patchy carbonate-rich units.

3.3.2. Reddish Clay-Enriched Layers (RCLs)

The RCLs are reduced to thin layers and exhibit clay contents of up to 84% (e.g., SL 5, sample 15), with clay representing the dominant grain-size fraction. In the upper RCLs (SL 3, 5, 7), a typical pattern is observed: the highest clay concentrations are found in the centre of the layer, while carbonate contents are lowest in this zone and increase toward the upper and lower boundaries. Hydromorphic features are widespread and include Fe-Mn concretions and Mn coatings on clay aggregates, often extending across both clay and carbonate-enriched layers. Elemental and mineralogical patterns vary among RCLs, and clear trends between them are difficult to identify. For instance, quartz values remain relatively constant throughout the section. Illite and kaolinite are present but do not follow a consistent distribution. Mn and Fe values fluctuate without a clear stratigraphic pattern.

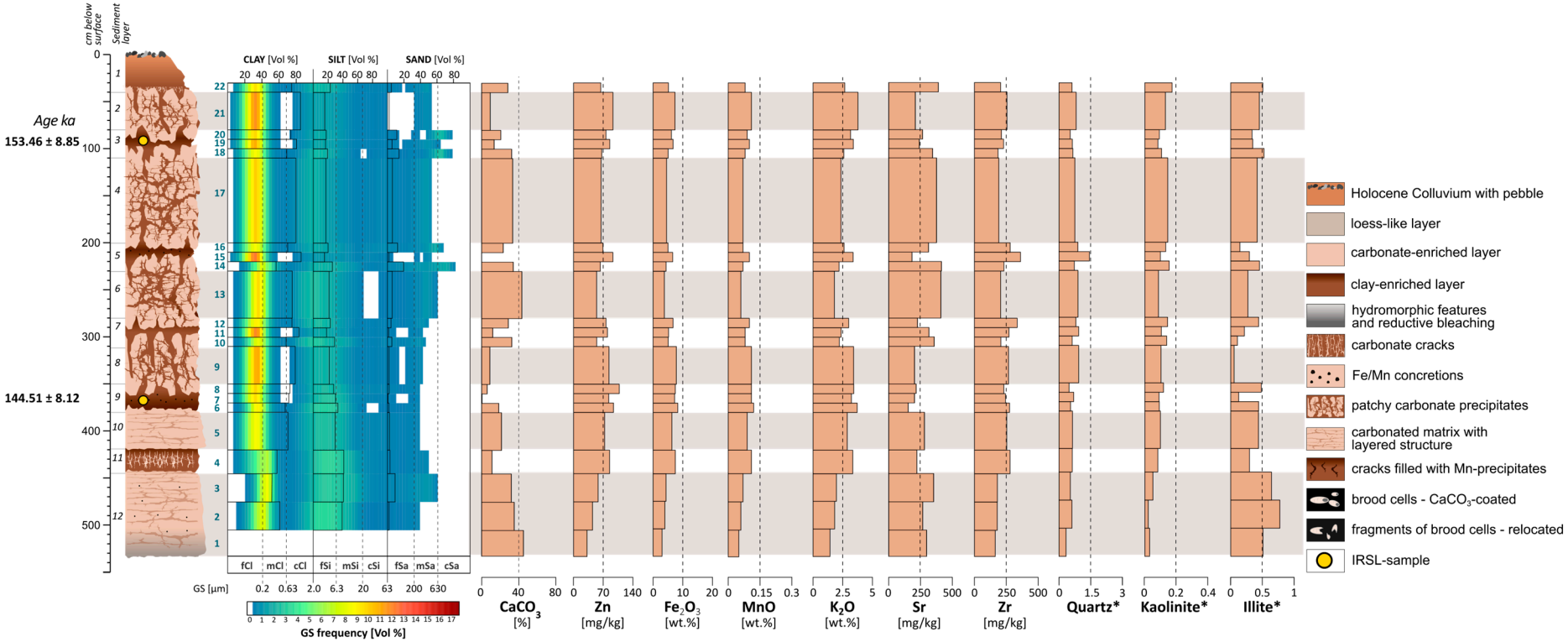

Figure 6. Section of Vallebrón with analytical data of the samples. Grain-size distributions are shown as heatmaps (frequency of a class in % Vol). Black lines show the cumulative percentage of clay, silt and sand. * Minerals are normalised to the sample-specific background and represent relative peak intensities.

3.3.3. Pale Carbonate-Enriched Layers (PCLs)

The carbonate-enriched layers are defined by their elevated $CaCO_3$ contents, reaching up to 45.4% in SL 12. While layers SL 2 to SL 8 show patchy carbonate enrichment, the more massive and consolidated layers SL 10 and SL 12 are clearly developed and laterally continuous. A separate grain-size analysis of the calcareous and clayey matrix components (Appendix A.2, Figure A1) reveals that secondary carbonate precipitates are associated with higher silt (>30%) and sand (up to 27%) contents, while the non-calcareous matrix shows high clay proportions (>60%). Fe-Mn concretions are also found in the carbonate layers, particularly in SL 12 and SL 10. Mn values do not show consistent vertical trends.

3.4. Luminescence Dating

Equivalent dose (De) distributions are generally narrow and approach normal distributions, indicating a high internal consistency of the luminescence data. Relative standard deviations are typically below 5%, and only a few samples show slightly skewed distributions, which are attributable to statistically significant outliers. These outliers were identified using a 1.5 IQR criterion and were not included in the De calculation based on the Central Age Model (CAM). All measured aliquots fulfilled the applied quality criteria and exhibited bright luminescence signals. Representative De distributions illustrating data quality and variability are shown in Appendix A.3 Figure A2. The IRSL ages obtained in this study are largely consistent with the OSL ages reported by von Suchodoletz et al. [16], showing recurrent Holocene and late Pleistocene dust deposition phases across the Femés and Teguise vega sections.

4. Discussion

4.1. Sediment Characteristics and Input Pathways into Vega Systems

4.1.1. Bedrock of the Catchment and Local Volcanism

Given the volcanic origin of the Canary Islands, the local volcanism with its input of tephra and lapilli should have an imprint on the vega systems. Surprisingly, no distinct tephra layers were identified in any of the studied sections. This absence is likely related to mixing within the fine-grained, clay-enriched deposits caused by peloturbation processes [17]. As a result, volcanic input is not preserved as stratigraphically distinct ash layers but is instead recorded indirectly through a pervasive basaltic geochemical background. This interpretation is supported by elevated Fe and Zn concentrations, which are characteristic of basalt-derived substrates on the eastern Canary Islands [45]. In both sections, these elements show systematically higher values in the reddish, clay-enriched RCLs than in the overlying PCLs, indicating a stronger geochemical influence of the basaltic substrate in these layers. In Teguise, this is particularly evident in SL 5, 7, and 9 (Figure 3), where Fe and Zn values remain high and stable over several decimetres. Comparable trends occur in Femés (SL 3, 5, 9; Figure 4), where Fe- and Zn-rich parts of the section coincide with the most clay-enriched layers. These Fe- and Zn-enriched RCLs frequently show very high clay contents exceeding 90% (e.g., SL 7 and 9 in Teguise, Figure 3; SL 3, 5, and 7 in Femés, Figure 4). Such extreme values are best explained by intense pedogenic overprinting within the valley floor, including clay neoformation (see Section 4.2). The associated rubefication, formation of new clay minerals, and elevated magnetic susceptibility values point to strong weathering processes [17], particularly in RCLs with a pronounced basaltic geochemical background, where the volcanic parent material likely facilitated enhanced alteration.

4.1.2. Aeolian Deposits

Aeolian sediments are characterised by high proportions of silt and clay, reflecting the preferential deposition of fine particles during atmospheric transport. In silty dust loads,

Zr concentrations are typically elevated [9,46], and quartz represents one of the most robust indicators of aeolian input on the eastern Canary Islands [5,27,28], as the local volcanic substrate lacks quartz. The close correspondence between Zr and quartz abundances in the Teguise (Figure 3) and Femés (Figure 4) sections, therefore, supports an aeolian origin of Zr and highlights its potential as a complementary proxy for dust deposition.

Several sediment layers in both sections show enrichments in these dust-related components. In Teguise, coincident maxima of silt, Zr, and quartz occur in layers SL 4, 6, 8, and 12. Layer SL 12 is particularly conspicuous due to its light grey colour, which initially suggested a possible tephra origin in the field. However, the absence of mafic minerals, together with low Fe and Zn contents and pronounced enrichments in quartz and Zr, clearly indicates an aeolian origin. In Femés, comparable peaks in dust indicators, especially quartz and Zr, are observed in SL 2 and SL 8, pointing to analogous phases of enhanced dust deposition.

Among these layers, SL 4 in Teguise and SL 2 in Femés near the surface stand out due to exceptionally high quartz and Zr values. Both correspond to the Holocene loess-like layer described by von Suchodoletz et al. [16], which has been interpreted as recording a short-lived episode of particularly intense dust input linked to increased anthropogenic land use in the Western Sahara. Beyond these prominent horizons, more subtle enrichments in quartz, Zr, and fine silt occur throughout the sequences, indicating that dust input was not limited to isolated events but constituted a recurrent process contributing to the progressive infill of the vegas.

Kaolinite provides an additional, though partly independent, indicator of aeolian input [13,27]. In the Teguise section, kaolinite reaches its highest values in layer 4, together with elevated quartz and Zr. Nevertheless, some RCLs—such as Teguise SL 9 and Femés SL 7—also contain increased kaolinite contents despite lacking peaks in the other dust proxies. This pattern indicates a more continuous supply of fine-grained dust components even during intervals when coarser silt deposition weakened. Illite, another mineral commonly associated with dust input from northern parts in North Africa [5,6,13,27], is also present in the vegas but shows no clear correspondence with other dust proxies. This decoupling may point to partial in situ formation or post-depositional alteration of this clay mineral (see Section 4.2). Carbonates also constitute a substantial component of Saharan dust [27], and the highest $CaCO_3$ contents in both sections coincide with silt-rich layers enriched in quartz and Zr, supporting an aeolian contribution. Within the vega systems, however, carbonates were subsequently redistributed, and the effects of this post-depositional mobilisation are discussed in more detail in Section 4.2.

4.1.3. Slope Deposits

The surrounding slopes of the catchments differ markedly in their inclination, which exerts a strong control on the potential for colluvial sediment input. Mean slope angles are approximately 10–12° around Teguise, 15–17° around Femés, and 12–13° around Vallebrón, with local maxima reaching up to 20°, 35°, and 30°, respectively. These differences provide an important geomorphological framework for interpreting site-specific variations in slope-derived contributions to the vega deposits.

Characteristic indicators of sediment input from former slope positions are fragments of calcified brood cells, which represent carbonate-cemented remains of originally intact nest chambers that became fragmented and redeposited during erosion and slope processes [47]. On the Canary Islands, such fragments have been widely used as indicators of sediment relocation, for instance within palaeodune archives [35]. Additional slope-indicative features include clay-rich soil aggregates, inclined layers or sub-layers near the slope–valley transition, and, locally, coarser stone fragments or pebble-rich horizons. These

coarse components are typical of Holocene colluvium at the surface (e.g., SL 1 in Femés and Teguise) but are absent from the lower parts of the sequences, indicating that slope-derived erosion was strongly reduced prior to the Holocene. In Femés, SL 6 shows abundant calcified fragments (Figure 4) and inclined bedding (Figure 5), pointing to enhanced colluvial dynamics, whereas in Teguise such features are scarce and the stratigraphy is dominated by massive, laterally continuous layers.

These site-specific differences can be explained by contrasting catchment morphologies. The steeper and longer slopes in Femés favour increased colluvial input, while the enclosed and gently inclined slopes around Teguise are comparatively short (typically <200 m) and terminate in a shallow upper valley close to the watershed. In this geomorphological position, the valley floor is only weakly incised, limiting the potential for slope-derived sediment delivery. Material supply in Teguise therefore mainly occurred through the reworking of pedogenic aggregates and fine colluvial sediments rather than through major erosional events, consistent with slope input characterised by high frequency but low magnitude [17]. Overall, slope deposits are largely restricted to fine-grained sediments, complementing in situ products of volcanic weathering and externally supplied aeolian dust as the principal sediment sources of the vegas, which were subsequently modified by post-depositional processes.

4.2. Post-Depositional Processes

4.2.1. Calcification Patterns

The alternation of pale carbonate-enriched layers (PCLs) and reddish clay-dominated layers (RCLs) indicates that de- and recalcification represent one of the most prominent post-depositional processes shaping the vega sequences. Carbonate dissolution and precipitation are expressed through a range of features, including fissure fills, crusts, and nodules, which document both vertical and lateral carbonate redistribution. The intensity and geometry of these features vary between sites and stratigraphic positions, reflecting differences in hydrological pathways and sediment properties.

Fissure fills provide clear evidence for vertical carbonate transport. In Femés, for example, SL 5 shows strongly developed vertical cracks filled with carbonate, whereas SL 7 exhibits a brick-like pattern of intersecting vertical and horizontal fissures (Figure 4). These geometries point to infiltration-driven precipitation of dissolved carbonate along structural weaknesses during periods of percolating water, a process typical of arid soils where secondary carbonates preferentially follow infiltration pathways [48]. Toward the PCLs, fissure fillings observed in underlying RCLs grade into increasingly massive carbonate accumulations. In both Teguise and Femés, these accumulations consolidate into dense, cemented layers interpreted as hardpan-like calcareous crusts, particularly in upslope positions. Their formation reflects repeated dissolution–precipitation cycles under vadose conditions, combined with the influence of slope-derived interflow, which mobilises dissolved carbonate and promotes its accumulation along layer boundaries. Such features correspond well with the inclined and laminated calcretes described from the eastern Canary Islands [49,50] and thus represent markers of cumulative carbonate redistribution within the vega systems.

Beyond vertical transport, lateral redistribution plays an important role in shaping carbonate patterns within the vegas. Interflow from surrounding slopes facilitates a diffuse transfer of dissolved carbonate into the valley floors, while capillary rise redistributes carbonate upward within fine-grained sediments with high water-holding capacity, producing diffuse impregnations and patchy accumulations [51]. This mechanism is well illustrated in layers such as SL 6 in Teguise (Figure 3) and SL 6 in Femés (Figure 4), where $CaCO_3$ contents increase upward. Repeated moisture fluctuations and capillary transfer, both

common drivers of calcrete formation [49,51], likely controlled these patterns. In some cases, increasing carbonate contents in SL 6 and 8 in Teguise and SL 10 in Femés may additionally reflect self-reinforcing precipitation dynamics, whereby ongoing cementation reduced porosity and permeability and thus enhanced further carbonate accumulation in overlying horizons. Such processes are most effective under relatively moist conditions, which we infer for transitional zones between PCLs and overlying RCLs, where desiccation cracking and intense recalcification frequently coincide (see Section 4.4).

The spatial distribution of carbonate enrichment further highlights the importance of sediment texture and catchment geometry. In the upper and middle parts of the Teguise sequence, massive carbonate accumulations are consistently associated with silt-rich layers, likely reflecting their higher hydraulic conductivity compared to clay-dominated horizons, which favoured interflow and carbonate precipitation. In contrast, the lower part of the sequence shows a different pattern. SL 11 in Teguise, despite elevated silt contents, lacks the massive carbonate overprinting observed in overlying PCLs such as SL 10. This discrepancy may be related to valley geometry and sedimentation dynamics: rapid infilling of the lower basin in a funnel-shaped catchment likely limited lateral water movement and reduced carbonate accumulation. Moreover, carbonate precipitation requires sufficient residence time of percolating or ponded water, so rapid sediment aggradation may have restricted or prevented the development of distinct calcareous horizons. Periods of weak or absent interflow may therefore be recorded in these intervals, while SL 10 marks the onset of more pronounced carbonate redistribution. Comparable phases may have occurred higher in the sequence but are probably condensed or obscured by later overprinting.

Finally, the close parallel between $CaCO_3$ and Sr contents provides additional insight into carbonate redistribution processes. Because Sr commonly substitutes for Ca in carbonate lattices [51,52], the near-identical trends of $CaCO_3$ and Sr in all carbonate-enriched layers in Teguise (SL 6, 8, 10) and Femés (SL 6, 8, 10) suggest that Sr is predominantly carbonate-bound and governed by the same dissolution–precipitation dynamics. The key issue is therefore not the covariance itself, but whether Sr enrichment primarily reflects aeolian input or secondary mobilisation. Carbonate-bearing dust from northern African source regions contains variable but generally low Sr concentrations, depending on the contribution of biogenic and pedogenic carbonates [13]. In addition, Sr-bearing biogenic carbonates from adjacent shelf areas of the eastern Canary Islands [30,53] may have been incorporated into the aeolian fraction. Alternatively, both Ca and Sr may have been mobilised after deposition, as carbonate phases are highly soluble under fluctuating moisture conditions. This interpretation is further supported by the presence of Sr in basaltic rocks, mainly hosted in plagioclase, providing an additional volcanic source for mobilised Sr [54]. Taken together, the redistribution of Ca and Sr underscores the dominant role of water in overprinting vega deposits, a control that extends beyond carbonate dynamics and is also reflected in hydromorphic and redox-related features.

4.2.2. Hydromorphic Features and Redox Processes

Hydromorphic overprinting is particularly evident in the lower parts of several PCLs in Teguise (SL 6, 8, 10), especially where they come into contact with underlying RCLs. These clay-enriched layers often act as semipermeable barriers, reducing vertical infiltration and promoting temporary water stagnation above them. Such conditions foster repeated redox fluctuations that mobilise manganese and iron, followed by reprecipitation once oxygen becomes available again [55,56]. These processes typically lead to the formation of Fe–Mn nodules and coatings, which are widely recognised as sensitive indicators of fluctuating hydrological regimes in soils [57].

In the vegas, these dynamics are recorded in the form of blackish fissure coatings and Mn-rich fillings, which clearly contrast with the carbonate-filled cracks observed in deeper parts of the RCLs in the sections of Teguise (SL 5, 7) and Femés (SL 5, 7, 9). This mineralogical differentiation highlights the importance of redox conditions in governing post-depositional transformations. Particularly striking are the manganese-coated insect nests (e.g., Anthophora-type) observed in Teguise (SL 6, SL 8) and Femés (SL 6). Their high density in the basal parts of PCLs, together with elevated Mn values, suggests that these parts were especially prone to short-term hydromorphic alteration before or during early carbonate enrichment. Pedogenic Mn-oxides typically form under such fluctuating redox conditions, precipitating as coatings on biological structures and soil aggregates [58].

Taken together, Mn-rich precipitates and coatings serve as sensitive indicators of short-term saturation and hydrological variability, complementing broader geochemical signals and showing that even brief wet–dry cycles can leave a lasting imprint on vega stratigraphy. The occurrence of such redox features implies periodically moist conditions within an otherwise semi-arid setting, possibly linked to episodic rainfall and interflow events led to transient waterlogging followed by rapid drying. These alternating reduction and oxidation phases reflect short-term fluctuations in moisture availability and indicate that vega formation occurred under highly variable hydrological conditions. Such repeated wetting and drying also promote clay mineral alteration and formation by alternating dissolution and reprecipitation, while the associated shrink–swell dynamics in clay-rich layers lead to peloturbation and structural reworking.

4.2.3. Clay Mineral Formation and Peloturbation

The exceptionally high clay contents of the RCLs—often exceeding 90%—result from several interacting processes rather than from primary sediment input alone. Reddish colouration, dense microstructures, and pervasive vertical and horizontal fissures indicate strong pedogenic overprinting under fluctuating hydrological conditions. Although soil formation on the valley floors was constrained by poor drainage and alkaline pH values [17], rubefication and a fine-textured, aggregate-rich structure point to pedogenic alteration, including clay mineral transformation and partial neoformation. Accordingly, the RCLs represent products of combined sediment accumulation and in situ modification. In contrast, less restricted slope positions likely provided more favourable conditions for soil development and thus acted as source areas for fine-grained, pedogenically modified material that was subsequently relocated to the valley floors.

Aeolian and colluvial inputs further contributed to the overall clay enrichment. Parts of the clay fraction—particularly kaolinite and illite—can be attributed to dust deposition (see Section 4.1), while local pedogenic processes added an authigenic component. Given the basaltic substrate of Lanzarote, in situ formation of smectite would be expected [59]. Although neither our XRD data nor previous studies [17] indicate significant smectite contents today, their former presence cannot be excluded. Smectites readily form on basaltic parent material and promote pronounced shrink–swell behaviour under alternating wet and dry conditions, providing a plausible explanation for the desiccation cracks characteristic of many RCLs. The vertical and brick-like cracking patterns observed in SL 7 at Teguise (Figure 3) and SL 5 at Femés (Figure 4) reflect such repeated moisture fluctuations, whereas layers lacking pronounced fissures, such as SL 9 in Teguise, likely record more stable and consistently dry conditions. Smectites may subsequently have undergone pedogenic illitisation driven by K fixation, a process well described in soil science [60], with elevated K concentrations in the RCLs supporting this interpretation without implying diagenetic conditions.

Authigenic formation of palygorskite has been reported from soils developed on Canary basalts [61,62] and palygorskite is also a common constituent of Saharan dust [13,25]. Despite these potential sources, palygorskite is absent in our XRD results. Its absence suggests that this mineral is unstable under the fluctuating hydrological conditions prevailing in the vegas. Repeated wetting and drying, combined with carbonate-rich pore waters, likely promoted its alteration and prevented long-term preservation. Consequently, the presence or absence of individual clay minerals within the vega deposits cannot be attributed solely to external dust input. Illite may partly reflect in situ transformation from smectite, whereas the disappearance of palygorskite points to continued mineral alteration under variable moisture regimes.

Hydrological fluctuations that promoted mineral transformation also induced pronounced shrink–swell dynamics, leading to cracking and pedogenic mixing (peloturbation) within the RCLs. Over time, many fissures became filled with carbonate or manganese, reducing further movement, while large clay aggregates preserved their internal structure. The degree of homogenisation therefore varies between layers. The RCL SL 7 at Teguise, for example, shows nearly identical luminescence ages over a thickness of about 1.2 m, indicating intense homogenisation, whereas most other RCLs retain clear internal differentiation. This is supported by variations in grain-size distributions as well as geochemical and mineralogical compositions (Figures 3 and 4). These observations demonstrate that although pedogenic processes significantly overprinted the clay-enriched layers, shrink–swell dynamics and peloturbation rarely resulted in complete homogenisation. As a consequence, aeolian dust signals are generally less well preserved in RCLs than in PCLs, but remain detectable even in strongly altered layers.

Figure 7 summarises the interaction of sediment sources, transport pathways, and post-depositional processes within the vega systems. Aeolian input affected the entire catchment, including both slopes and valley floors, where it mixed with volcanic material and shelf-derived components. On the slopes, clay neoformation and transformation, weathering of bedrock, and alternating de- and recalcification processes produced fine-grained soil material that was subsequently translocated downslope by runoff and interflow. On the valley floors, deposition occurred under alternating standing-water and dry conditions, promoting clay transformation, partial destruction, shrink–swell cycles, and repeated carbonate redistribution through crack filling. Together, these coupled processes generated the characteristic alternation of clay- and carbonate-enriched layers and the internal differentiation observed within the vega sequences.

4.3. Impact of Volcanic Damming on Sedimentation and Archive Quality

Vallebrón, where the catchment is drained, preserves largely homogeneous clay-enriched deposits with patchy and diffuse carbonate enrichments (Figures 2C, 6 and A1). Proxy data confirm this homogenisation: quartz, silt, and Zr—indicating aeolian input—show little variability throughout the section. Nevertheless, the persistence of clay-enriched layers together with Mn-enriched features suggests repeated phases of increased soil moisture, resulting in hydromorphic overprinting. The Vallebrón section illustrates that undammed sites, comparable to dammed vega systems, can still record phases dominated by alternating dry and wet conditions, as indicated by the abundant carbonate-filled cracks. The consistently high clay contents throughout the section indicate that most of the fine material was transported from upslope areas or deposited directly by dust input, and temporarily settled under standing-water conditions within the valley floor. Such conditions allowed clay to accumulate from suspension, pointing to the dominance of reworked soil sediments transported through the valley rather than to in situ clay

neoformation, which would typically produce an upward increase in clay content towards the former surface.

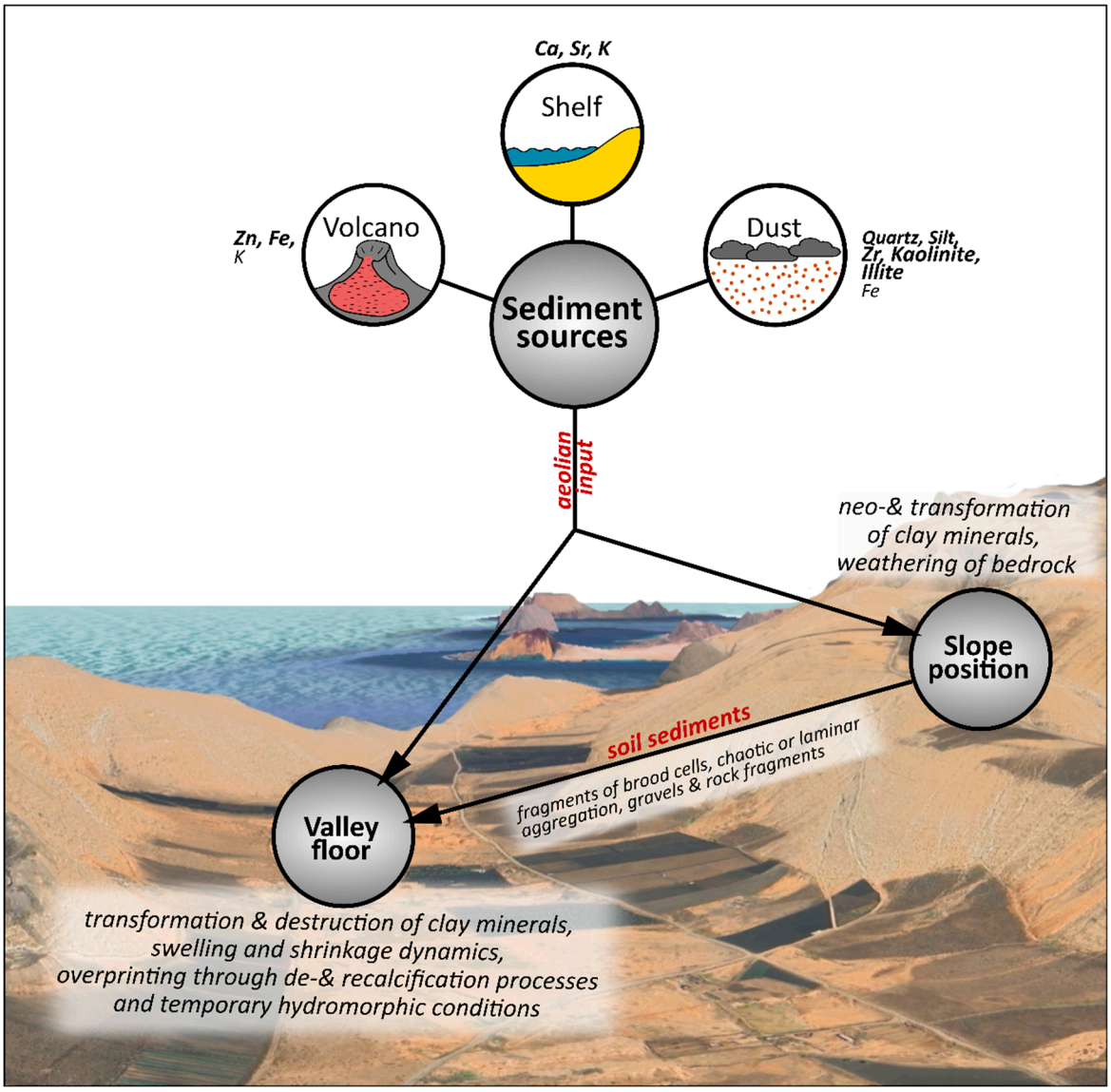

Figure 7. Illustrating dust dynamics and the interaction of different sediment sources, their elemental or mineralogical indicators (bold), and transport pathways into the vegas. The background image shows a satellite view of the vega catchment of Teguise (source: Google Earth).

Femés, in contrast, represents a dammed system but is characterised by a significantly steeper relief compared to Teguise and Vallebrón. Here, sediment transport from the slopes remained more pronounced than in Teguise. The strong influence of the steeper slopes is further reflected in the frequent occurrence of calcified brood-cell fragments (e.g., SL 5/6; Figure 4), which document enhanced colluvial input. In several stratigraphic positions, converging and overlapping layers complicate straightforward correlations between different outcrops within the opencast area. With respect to dust indicators, the PCLs do not consistently exhibit parallel peaks in quartz, silt, and Zr; such patterns are confined to SL 8 and the loess-like layer SL 2. Femés thus demonstrates that volcanic damming generally improves stratigraphic preservation, while the steeper catchment morphology favours a more complex internal stratigraphy with distinct sublayers, reducing the clarity with which aeolian dust signals are preserved.

Teguise, with its almost completely dammed basin and low slope-to-valley ratio is characterised by laterally continuous layers of nearly constant thickness and horizontal stratification over several tens of metres (Figures 2A and 3), indicating deposition under low-energy, partly standing-water conditions that promoted the settling of fine-grained material. The scarcity of features such as erosional contacts, channel structures, or coarse-grained layers or lenses, together with coherent geochemical and mineralogical patterns, points to limited colluvial input. The horizontal layering observed on the valley floor can be traced laterally onto the adjacent slopes, where individual RCLs and PCLs gradually thin out with increasing elevation (Figure 8). The loess-like layer (SL 4) also maintains lateral continuity but becomes progressively thinner upslope. These relationships suggest that sedimentation extended beyond the central basin floor and that low-energy depositional conditions prevailed even along the lower slopes, forming laterally coherent strata rather than discrete slope-derived layers.

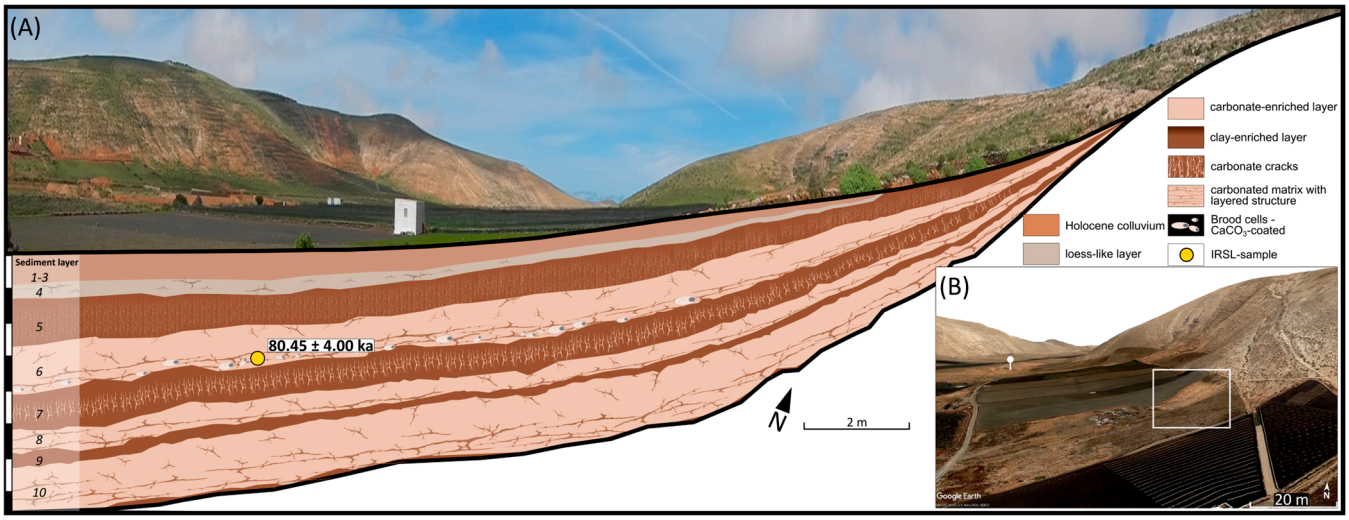

Figure 8. (**A**) Stratification within the valley floor and up to the slopes in Teguise, showing progressive thinning of sediment layers with increasing elevation. (**B**) Oblique aerial view and catchment map illustrating the location of the documented slope section within the upper Teguise catchment. The slope section is marked by white rectangles, while the position of the valley floor section is indicated by white location pins (Source: Google Earth).

The cyclic alternation of PCLs and RCLS is most clearly expressed in Teguise, both visually in the outcrop and in the proxy data, where shifts in grain size, elemental composition, and mineralogy define repeated dust–soil formation cycles. Primary dust signals are especially well preserved in the lower parts of PCLs (e.g., SL 6; Figure 3), where quartz, silt, and Zr contents peak in parallel, and in the distinct loess-like layer SL 4 with sharp boundaries and maximum dust-proxy values. Stable Fe and Zn backgrounds in RCLs and carbonate restricted to vertical fissure fillings (Section 4.2) further underline the integrity of the sequence. Taken together, Vallebrón stores information about moisture fluctuations under drained conditions, Femés illustrates the dynamics caused by steeper slopes, and Teguise highlights the capacity of dammed low-relief basins to preserve continuous, cyclic dust archives.

In a broader context, the vega deposits can be related to other small endorheic basins in arid to semi-arid regions, which are commonly characterised by sedimentation and post-depositional modification. Conceptual frameworks for arid landscapes emphasise that sediment accumulation in such basins is controlled by episodic hydrology, aeolian input, slope-derived material, and pedogenic processes rather than by continuous lacustrine deposition [63]. Studies on pans and playas show that alternating phases of flood-

ing and drying typically produce successions of contrasting clay-rich and carbonate- or salt-enriched layers that are subsequently overprinted by soil formation and secondary redistribution [64]. Recent work further highlights that small endorheic basins act as sensitive but strongly filtered recorders of regional environmental change, requiring a process-based interpretation of dust and hydrological signals [65]. In contrast to many exposed pans and playas, the vega systems appear to provide a comparatively continuous sedimentary archive. Their sheltered valley-floor position, the dominance of fine-grained, clay-rich sediments, and the lack of evidence for significant deflation or erosive truncation indicate that sediment export from the vega systems was strongly limited prior to the Holocene, whereas the occurrence of gravel- and pebble-rich layers documents enhanced erosion.

In addition, the proxy data from the Teguise section, but partly also from Femés, allow for an extended interpretation of vega formation. The pronounced peaks in quartz, Zr, and silt within the Holocene loess-like layer of Teguise and Femés reflect short-lived but high-intensity dust deposition events. While the Holocene loess-like layer was previously interpreted as a singular record of exceptional dust input, possibly linked to early human activity in the Northwest Sahara [19], the recurrence of similar layers within the late Pleistocene sequences argues against this view. Instead, the proxy patterns suggest that these deposits represent repeated phases of system shifts, during which enhanced dust mobilisation was followed by renewed processes of soil formation under fluctuating hydrological conditions. The Holocene loess-like layer is therefore not a singularity but rather the latest expression of a recurring system shift that has characterised vega formation since at least the late Pleistocene.

4.4. Vega Formation

When taking a closer look at the alternation of PCLs and RCLs, we interpret the succession of one sequence (one PCL overlain by one RCL) as follows:

One sequence (Figure 9a) begins with the deposition of silt-dominated material (also increased in the content of fine sand) and enriched in quartz and Zr. We interpret that deposit as a kind of "dust event" in the sense of a shorter period (only hundreds to thousands of years), since luminescence dating of the Holocene loess-like layer indicates a brief depositional phase. Ages of 6.4 ± 0.7 ka (Femés) and 7.2 ± 0.8 ka (Teguise) from von Suchodoletz et al. [16], together with 4.86 ± 0.26 ka and 5.57 ± 0.30 ka from this study, confirm deposition within a narrow time window of this dust input. These silt-dominated deposits have a significantly higher coefficient of water permeability in contrast to all layers dominated by very high clay contents.

When these deposits overlie clay-enriched sediments with a very low coefficient of permeability, vertical water infiltration becomes impeded, resulting in the formation of temporary waterlogged zones that favour carbonate mobilisation and reprecipitation (Figure 9b–c). Dissolved carbonates, supplied both by the dust itself and by slope-derived contributions, precipitate along cracks and pore spaces, gradually forming calcareous crusts, resulting in cementation. Infiltration, capillary rise, and lateral interflow together enhance the redistribution of carbonates, with interflow favouring lateral enrichment by transporting dissolved carbonates along layer boundaries between one RCL and an overlying PCL [49,50]. Short-term hydromorphic conditions in the basal parts also promote Fe–Mn precipitation, forming manganese coatings around insect brood cells as observed in the Teguise and Femés sections.

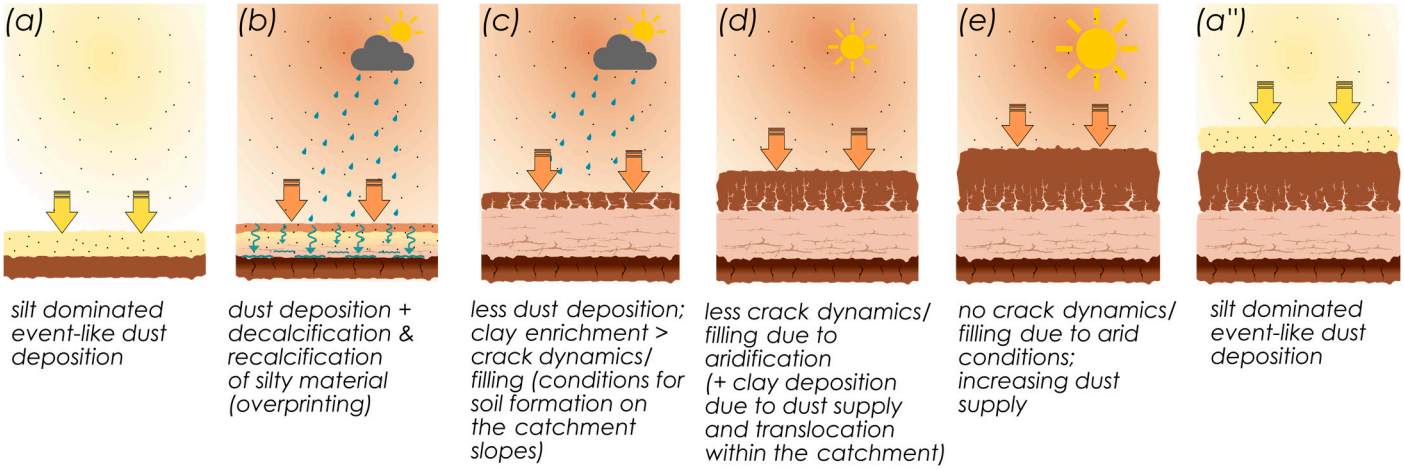

Figure 9. Generalised conceptual model of cyclic vega formation showing dust deposition (**a**); carbonate redistribution (**b**,**c**); clay enrichment (**d**); transition to the next dust input phase (**e**,**a"**).

The subsequent development (Figure 9b,c) is characterised by (1) a change in dust composition towards finer, clay dominated sediments, in combination with decreasing contents in quartz and Zr but persistent kaolinite; (2) in situ transformation of clay, possibly involving smectite alteration to illite under K-rich conditions (to some extent, neoformation of clay may also be contributing); and (3) colluvial input of clay-dominated (soil) sediments from the slopes. Repeated wetting and drying cycles cause shrinking and swelling dynamics within the clay-dominated material (Figure 9c), generating vertical cracks and promoting peloturbation.

When drier conditions occur, carbonate redistribution and hydromorphic activity diminish, and clay-enriched layers stabilise (Figure 9e). Assumingly, the sedimentation rate decreases, but in many RCLs the upper parts already show increasing quartz and Zr contents, signalling the onset of a new dust event and foreshadowing the next cycle.

A subsequent dust event (Figure 9a") again deposits silt-dominated material enriched in quartz and Zr on top of the formed RCL. If reworked under moist conditions, these sediments follow the same pathway, producing the characteristic alternation of PCLs and RCLs that characterise the vega archives.

To complement the conceptual model of vega formation (Figure 9), we compiled a quantitative synthesis of grain-size fractions and selected proxies using sample-based median values for the main sedimentary units at both sites (Figure 10). These medians show that loess-like layers are characterized by the highest silt contents and elevated quartz and kaolinite signals compared to the underlying PCL, whereas RCLs are dominated by high clay contents and elevated Zn concentrations.

These contrasts imply that the observed alternations are driven by changes in regional dust supply and associated climatic boundary conditions. The dust event deposits must be linked to enhanced dust mobilisation in North Africa. Those shifts could be monsoon-driven or caused by glacial–interglacial transitions or high-latitude cold events [10,66,67]. The IRSL ages from Teguise and Femés indicate that major dust events occurred at around 111 ka, 92 ka, and ~5 ka, each representing periods of intensified aeolian input followed by phases of pedogenic overprinting, while intervening RCLs (~84–88 ka, ~132 ka) reflect finer dust input, clay neo- or transformation, or colluvial input. These alternations underline the cyclic nature of the vega sequences and suggest that the Holocene loess-like layer represents the youngest expression of a recurring system shift rather than an isolated event.

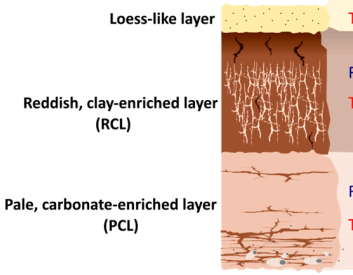

	Site (medians)	Clay %	Silt %	Sand %	Zn (mg/kg)	Quartz*	Kaolinite*	samples
Loess-like layer	Femés	38.32 [34.38–42.26]	**59.33** [55.40–63.27]	2.34 [2.34–2.35]	93.25 [92.62–93.88]	**2.24** [2.07–2.41]	**0.10** [0.09–0.11]	2 *
	Teguise	44.80 [37.63–52.09]	**49.47** [43.62–54.47]	**6.93** [5.50–7.90]	67.85 [62.50–83.78]	**3.45** [2.75–3.61]	**0.10** [0.08–0.12]	4 *
Reddish, clay-enriched layer (RCL)	Femés	**78.57** [73.80–82.60]	20.03 [16.53–25.65]	1.01 [0.45–1.70]	**101.50** [95.90–104.75]	0.75 [0.62–0.92]	0.05 [0.03–0.07]	30
	Teguise	**86.33** [83.55–90.63]	13.43 [9.14–15.45]	0.09 [0.00–1.40]	**98.00** [91.50–103.75]	0.85 [0.62–1.12]	0.07 [0.06–0.08]	30
Pale, carbonate-enriched layer (PCL)	Femés	56.77 [43.74–66.26]	39.34 [32.43–50.93]	**3.12** [1.88–6.20]	86.20 [79.45–91.10]	0.70 [0.55–1.32]	0.05 [0.04–0.06]	15
	Teguise	74.27 [62.78–83.75]	24.34 [16.25–35.21]	0.43 [0.05–1.50]	72.30 [65.90–77.85]	0.83 [0.57–1.17]	0.05 [0.04–0.06]	27

Figure 10. Typical vega sequence and sample-based median values of grain size fractions and selected geochemical proxies for the Teguise and Femés section. Median values are calculated by pooling all samples belonging to a given site and layer type; brackets indicate the interquartile range (Q25–Q75). Bold values indicate the highest values in both vega sections for grain sizes and other proxies. Quartz and kaolinite are shown as relative peak intensities normalized to the sample-specific background. Numbers indicate the total number of samples per category. Asterisks (*) indicate loess-like layers with very low sample numbers ($n \leq 4$), where median values may be interpolated and are not statistically robust.

Marine sediment records from the North Canary Basin document orbitally forced variability in dust supply, grain size, and productivity, which has been linked to changes in trade-wind intensity and aridity in northwestern Africa [68]. These records indicate pronounced contrasts between glacial and interglacial boundary conditions and highlight the role of precession-paced modulation of aeolian transport pathways. While the timing of individual dust events identified in the vega sequences does not allow a direct temporal correlation with specific features in the marine records, the vega archives reflect repeated alternations between phases of dust accumulation and subsequent pedogenic overprinting, a pattern that is compatible with the orbitally forced variability in dust supply documented for the North Canary Basin.

Enhanced dust supply from northern Africa has frequently also been associated with the breakdown of African Humid Periods (AHPs), when vegetation retreated and increased aridity promoted dust mobilisation [10,64]. Such precession-paced changes in monsoon strength were likely further modulated by obliquity-controlled variations in North Atlantic sea-surface temperatures and associated shifts in westerly circulation [18]. Higher obliquity phases appear to have favored increased moisture availability on Lanzarote, whereas lower obliquity promoted drier conditions and enhanced dust fluxes. The vega sequences may therefore integrate both monsoon-driven dust input variability and obliquity-modulated hydrological changes, capturing the combined influence of tropical and high-latitude forcing on sediment formation in the eastern Canary Islands. However, short-lived climatic perturbations such as Heinrich Events are probably obscured by post-depositional mixing through peloturbation within the clay-enriched units.

In a next step, further dating and geochemical fingerprinting will aim to better constrain the drivers of recurring dust events and to disentangle palaeoclimatic conditions in the dust source areas relative to those on the eastern Canary Islands.

5. Conclusions

The vega sections of Lanzarote demonstrate that loess-like layers are not isolated anomalies but recur throughout the stratigraphy. Many PCLs originated as loess-like dust deposits that were subsequently transformed by secondary carbonate redistribution, meaning that these horizons represent masked records of short-lived dust events. The alternation of PCLs and RCLs captures cyclic environmental changes, with PCLs reflect-

ing phases of enhanced aridity and dust mobilisation, and RCLs recording intervals of finer dust input and increased soil-forming activity, partly supported by colluvial supply from the surrounding slopes under more humid conditions. This duality highlights two distinct dust signals preserved in the vegas: episodic pulses of coarse dust fall, and the more continuous input of fine-grained material, particularly detectable through kaolinite in RCLs. Clay mineral transformations further complicate provenance signals. Elevated potassium concentrations may have promoted the conversion of smectite to illite, implying that illite in the vegas can derive both from Saharan dust and from in situ alteration. Palygorskite, by contrast, appears unstable under the hydrological conditions of the valley floors and is largely absent despite potential aeolian and pedogenic sources. The geomorphological setting exerts additional control on archive quality. Drained catchments such as Vallebrón mainly preserve signals of pedogenesis and hydrological variability, while dammed basins capture more continuous stratigraphies. Among these, Teguise provides the clearest expression of cyclic dust fall and post-depositional modification, underscoring the value of volcanic damming in enhancing archive continuity. At the same time, sediment mixing due to peloturbation limits the temporal resolution of the archives, preventing the detection of short-lived events such as Heinrich Events. Nevertheless, the sequences reliably register major phases of dust mobilisation and alternating arid–humid conditions. The timing of these phases broadly aligns with orbitally paced monsoon variability, and arid intervals may be linked to the termination of African Humid Periods.

Taken together, the vegas of Lanzarote preserve both the magnitude and cyclicity of Late Quaternary dust deposition, while also recording the pedogenic and hydrological processes that overprinted these signals. They thus provide valuable archives for reconstructing dust–climate interactions in subtropical environments.

Author Contributions: Conceptualization, D.F. and C.-B.R.; methodology, T.K., A.M.S. and C.G.; investigation, J.L., D.F., C.-B.R., T.K. and C.M.; writing—original draft preparation, J.L.; writing—review and editing, all authors; visualization, J.L.; project administration, D.F. and C.-B.R.; funding acquisition, D.F. All authors have read and agreed to the published version of the manuscript.

Funding: This research was funded by the German Research Foundation (FA239/26-1).

Data Availability Statement: Available upon request.

Acknowledgments: We are very thankful to Hans von Suchodoletz for the open and fruitful discussions and for the provision of samples that enabled us to start laboratory work during the restrictions imposed by the pandemic—many thanks! We are also grateful to Inmaculada Menéndez and Anna Pint for their support in coordinating the fieldwork and for the constructive exchange during the project. Special thanks go to Beate Winkler and Christiane Grafe for the laboratory measurements at TU Dresden, and to Gunnar Pruß for organising the grain-size analyses at GFZ. We would also like to thank Christiane Richter and Daniel Wolf for their constructive comments during the preparation of this manuscript, as well as Michael Zech for the helpful discussions and his support in this study. Special thanks go to the three anonymous reviewers for all their comments and advice. We gratefully acknowledge funding by the German Research Foundation (FA239/26-1).

Conflicts of Interest: The authors declare no conflicts of interest.

Abbreviations

The following abbreviations are used in this manuscript:

BCs	Brood Cells (brood chambers of ground-nesting Anthophora bees)
PCL	Pale, carbonate-enriched layer
PSA	Potential source area
RCL	Reddish, clay-enriched layer
SAL	Saharan Air Layer
SL	Sediment layer
XRD	X-ray diffraction
XRF	X-ray fluorescence
IRSL	Infrared stimulated luminescence

Appendix A

Appendix A.1

Table A1. Sediment layers of the Vega Teguise.

Sediment Layer	Description	Dominant Grain Size	$CaCO_3$	Higher Values of	Lower Values of	Redoximorphic Features	Pedofeatures or Relocation Features	BCs
SL 1	Colluvial layer	Silt (48%)	<10.2%				Bands of gravels, rock fragments on top	
SL 2	RCL	Clay (>61%)	<9% (decrease from top to base)				Gravels at the base	
SL 3	Clayey-silty layer	Clay (<62%), silt (<48%)	<4%					
SL 4	Loess-like layer	Silt (<60%)	<0.8%	Peaks of Quartz, Kaolinite, Zr, Mn	Zn, $CaCO_3$	Fe-Mn concretions		Residues of calcified BCs or manganised inlets
SL 5	RCL	Clay (<92%), higher amounts of silt in upper parts	<6%	Zn; in upper parts: Quartz, Zr, Mn	Sr, $CaCO_3$; in lower parts: Quartz, Zr, Mn	Mn-precipitates along fissures in upper parts	Vertical carbonate cracks	
SL 6	PCL	Clay (<89%), higher amounts of silt in lower parts	<33%, lower amounts in lower parts	$CaCO_3$, Sr; in lower parts: peaks of Quartz, Zr, Mn	Zn; in upper parts: Quartz, Zr, Mn	In lower parts Fe-Mn concretions	Compact, horizontal calcareous layers at the base	In lower parts, residues of calcified BCs or manganised inlets
SL 7	RCL	Clay (<93%), higher amounts of silt in upper parts	<4%	Zn; in upper parts: Quartz, Zr, Mn	Sr, $CaCO_3$; in lower parts: Quartz, Zr, Mn	Mn-precipitates along fissures	Vertical carbonate cracks	
SL 8	PCL	Clay (<80%) in upper parts, silt in lower parts (<60%)	<32%, lower amounts in lower parts	$CaCO_3$, Sr; in lower parts: peaks of Quartz, Zr, Mn	Zn; in upper parts: Quartz, Zr, Mn	In lower parts, Fe-Mn concretions	Compact, horizontal calcareous layers at the base	In upper parts, residues of calcified BCs or manganised inlets
SL 9	RCL	Clay (<95%)	Absent	Zn, Illite, Kaolinite; in	Quartz, Sr, Mn	Mn-precipitates along fissures		
SL 10	PCL	Clay (<90%), higher amounts of silt in lower parts	<45%	$CaCO_3$, Sr (peak at the base)	Zr	In lower parts Fe-Mn concretions	Compact, horizontal calcareous layers at the base	
SL 11	Clayey-silty layer	Clay (<72%), silt (<53%)	<14%	Zn, Zr	Sr	Mn-precipitates along fissures	Vertical carbonate cracks	
SL 12	Loess-like layer	Clay (<57%), silt (46%)	<2%	Quartz (peak), Kaolinite, Zr (peak)	Mn, $CaCO_3$	Fe-Mn concretions		

Table A1. *Cont.*

Sediment Layer	Description	Dominant Grain Size	$CaCO_3$	Higher Values of	Lower Values of	Redoximorphic Features	Pedofeatures or Relocation Features	BCs
SL 13	Clayey layer with redoxi-morphic features	Clay (<78%)	<0.8%	Zn, Mn	Sr	Fe-Mn concretions, increasing bleaching downwards		
SL 14	Silt-enriched layer	Silt (<56%)	<15%	Sand, Sr	Illite, Kaolinite			

Table A2. Sediment layers of the Vega Femés.

Sediment Layer	Description	Dominant Grain Size	$CaCO_3$	Higher Values of	Lower Values of	Redoximorphic Features	Pedofeatures or Relocation Features	BCs
SL 1	Colluvial layer	Silt (<57%)	<6%					
SL 2	Loess-like layer	Silt (<67%)	<3.2%	Peaks of quartz, Zr	Mn			
SL 3	RCL	Clay (<82%)	<8%	Zn; in upper parts: Quartz, Kaolinite, Illite	Sr		Fissures, fossil roots	
SL 4	Clayey-silty layer	Clay (<74%)	<13.6%	$CaCO_3$		Fe-Mn concretions		Residues of calcified BCs or manganised inlets
SL 5	RCL	Clay (<92%)	<4.8%	Zn, Mn	Sr	Band in form of Fe-Mn concretions at the base	Small vertical carbonate cracks in upper part, big carbonate cracks in lower part	
SL 6	PCL	Clay (<78%), higher amounts of silt (<58%) in lower parts	<21.3%	$CaCO_3$, Sr	Quartz, Zn	Fe-Mn concretions		Residues of calcified BCs or manganised inlets
SL 7	RCL	Clay (<78%)	<12.7%	Zn, Zr	Sr	Fe-Mn concretions	Horizontal calcareous layers in upper part, vertical and horizontal cracks in lower part	
SL 8	PCL	Silt (<60%)	<12.1%	$CaCO_3$; peaks of quartz, Zr, Sr	Zn	Fe-Mn concretions		
SL 9	RCL	Clay (<89%)	<25%	Zn	Quartz, Sr	Mn-precipitates along fissures, Fe-Mn concretions	Vertical carbonate cracks	
SL 10	PCL	Clay (<84%), silt (<52%)	<36.5%	$CaCO_3$, Sr		Fe-Mn concretions		
SL 11	Clayey-silty layer	Clay (<59%), silt (<40%)	<4%	Zn		Fe-Mn concretions		

Table A3. Sediment layers of the catchment Vallebrón.

Sediment Layer	Description	Dominant Grain Size	$CaCO_3$	Higher Values of	Lower Values of	Redoximorphic Features	Pedofeatures or Relocation Features	BCs
SL 1	Colluvial layer	Clay (<73%)	28.5%	Kaolinite, Sr				
SL 2	Clayey, carbonate-enriched layer (patchy)	Clay (<83%)	9.3%		Sr			
SL 3	RCL—Clayband	Clay (<78%)	Transition areas: <32.7%, Central layer: 13.6			Fe-Mn concretions		
SL 4	Clayey, carbonate-enriched layer (patchy)	Clay (<78%)	33.7%					
SL 5	RCL—Clayband	Clay (<84%)	Transition areas: <19.6%, Central layer: 0		$CaCO_3$	Fe-Mn concretions		

Table A3. *Cont.*

Sediment Layer	Description	Dominant Grain Size	$CaCO_3$	Higher Values of	Lower Values of	Redoximorphic Features	Pedofeatures or Relocation Features	BCs
SL 6	Clayey, carbonate-enriched layer (patchy)	Clay (<73%)	43.7%					
SL 7	RCL—Clayband	Clay (<81%)	Transition areas: <32.8%, Central layer: 12.1%		$CaCO_3$			
SL 8	Clayey, carbonate-enriched layer (patchy)	Clay (<77%)	9%					
SL 9	Clayband	Clay (<70%)	Transition areas: <19%, Central layer: 0.4%	Zn	$CaCO_3$, Illite	Fe-Mn concretions		
SL 10	PCL	Clay (<69%)	21.6%					
SL 11	RCL—Clayband	Clay (<55%)	11.2%		$CaCO_3$		Vertical carbonate cracks	
SL 12	PCL	Clay (<60%)	<45.4%			Fe-Mn concretions		

Appendix A.2

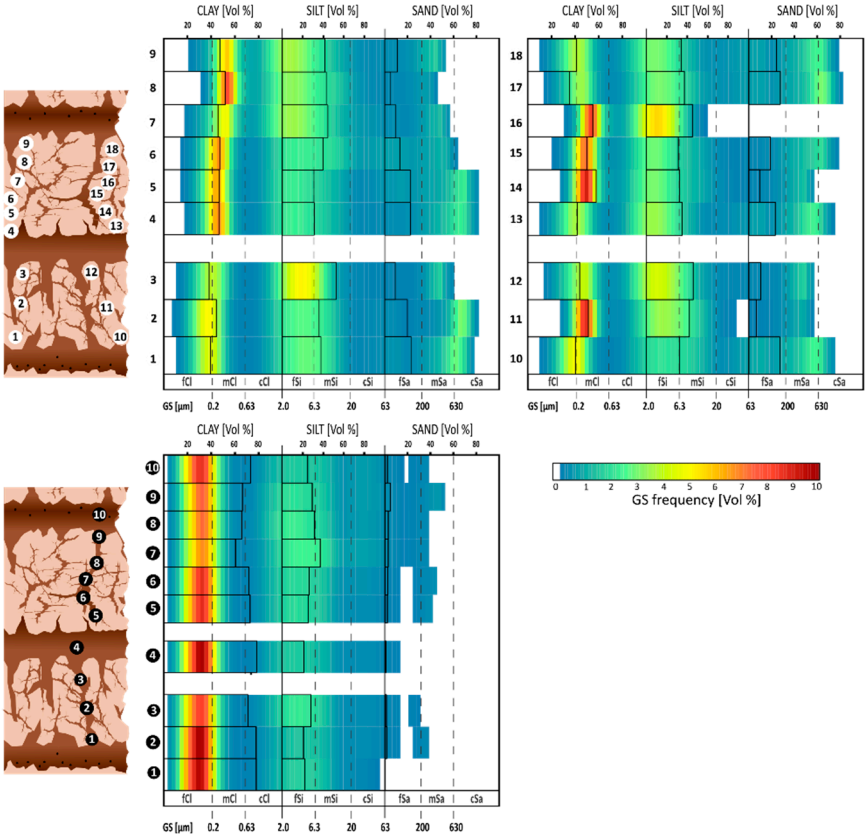

Figure A1. Grain-size distribution of samples from Vallebrón. Upper panels show samples from secondary carbonate-filled cracks, lower panel shows samples from the clay-rich matrix material. Data are presented as heatmaps of relative grain-size proportions, ranging from very fine clay (fCl) to coarse sand (cSa). The matrix samples, obtained from additional and spatially higher-resolved sampling, display a remarkably uniform texture dominated by fine clay and clayey silt fractions, indicating limited vertical variability.

Appendix A.3

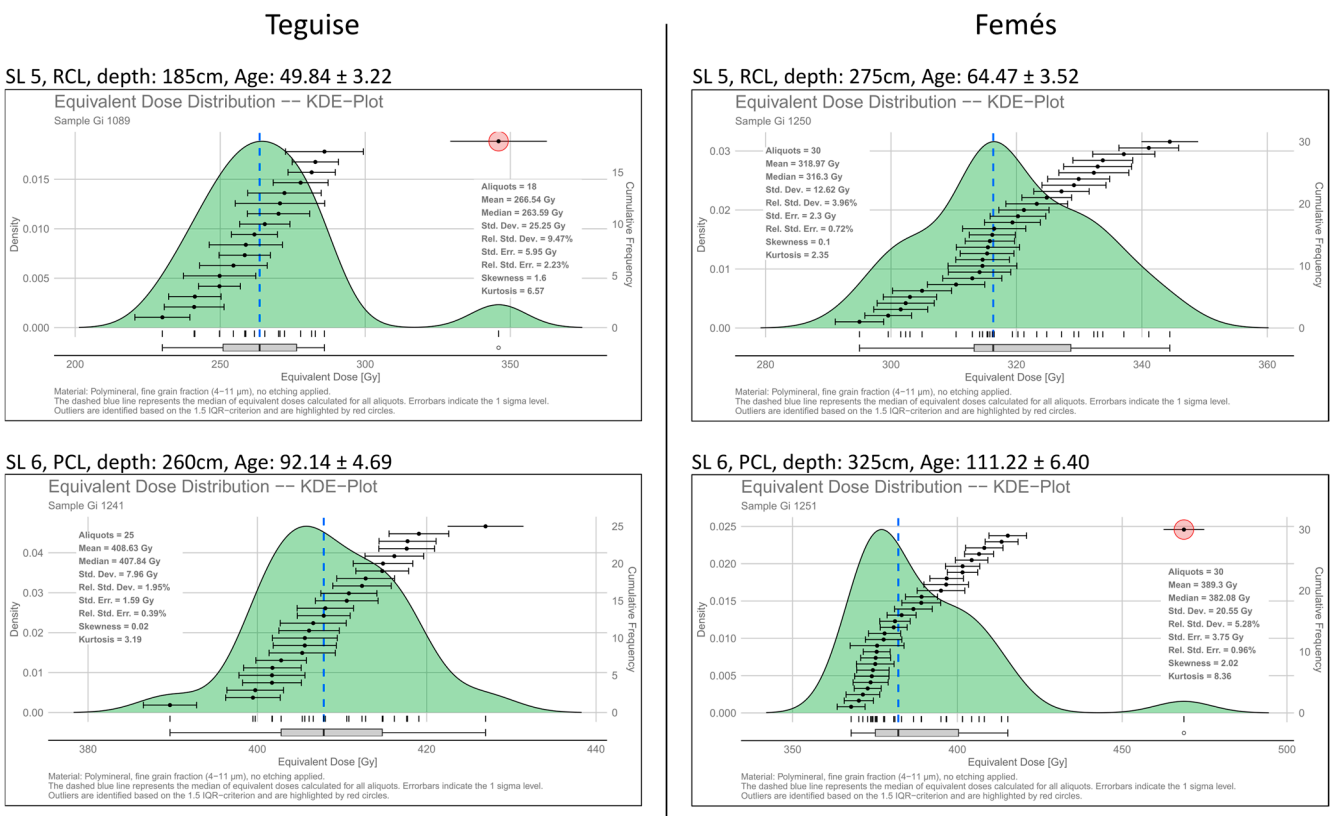

Figure A2. Representative equivalent dose (De) distributions for selected luminescence samples shown as kernel density estimate (KDE) plots. The dashed blue line marks the CAM median De value; outliers identified using the 1.5 IQR criterion are highlighted. The plots illustrate the generally narrow De distributions and the high internal consistency of the luminescence data.

References

1. Prospero, J.M. Long-Range Transport of Mineral Dust in the Global Atmosphere: Impact of African Dust on the Environment of the Southeastern United States. *Proc. Natl. Acad. Sci. USA* **1999**, *96*, 3396–3403. [CrossRef] [PubMed]
2. Schulz, M.; Prospero, J.M.; Baker, A.R.; Dentener, F.; Ickes, L.; Liss, P.S.; Mahowald, N.M.; Nickovic, S.; García-Pando, C.P.; Rodríguez, S.; et al. Atmospheric Transport and Deposition of Mineral Dust to the Ocean: Implications for Research Needs. *Environ. Sci. Technol.* **2012**, *46*, 10390–10404. [CrossRef] [PubMed]
3. Pouillé, S.; Talbot, J.; Tamalavage, A.E.; Kessler-Nadeau, M.É.; King, J. Impacts of Mineral Dust on Trace Element Concentrations (As, Cd, Cu, Ni and Pb) in Lichens and Soils at Lhù'àän Mân' (Yukon Territory, Canada). *J. Geophys. Res. Biogeosci.* **2024**, *129*, e2023JG007927. [CrossRef]
4. Bachelder, J.; Cadieux, M.; Liu-Kang, C.; Lambert, P.; Filoche, A.; Galhardi, J.A.; Hadioui, M.; Chaput, A.; Bastien-Thibault, M.-P.; Wilkinson, K.J.; et al. Chemical and Microphysical Properties of Wind-Blown Dust near an Actively Retreating Glacier in Yukon, Canada. *Aerosol Sci. Technol.* **2020**, *54*, 2–20. [CrossRef]
5. Muhs, D.R. The Geologic Records of Dust in the Quaternary. *Aeolian Res.* **2013**, *9*, 3–48. [CrossRef]
6. Formenti, P.; Schütz, L.; Balkanski, Y.; Desboeufs, K.; Ebert, M.; Kandler, K.; Petzold, A.; Scheuvens, D.; Weinbruch, S.; Zhang, D. Recent Progress in Understanding Physical and Chemical Properties of African and Asian Mineral Dust. *Atmos. Chem. Phys.* **2011**, *11*, 8231–8256. [CrossRef]
7. Neff, J.C.; Ballantyne, A.P.; Farmer, G.L.; Mahowald, N.M.; Conroy, J.L.; Landry, C.C.; Overpeck, J.T.; Painter, T.H.; Lawrence, C.R.; Reynolds, R.L. Increasing Eolian Dust Deposition in the Western United States Linked to Human Activity. *Nat. Geosci.* **2008**, *1*, 189–195. [CrossRef]
8. Kohfeld, K. Record of Mineral Aerosols and Their Role in the Earth System. *Treatise Geochem.* **2007**, *4*, 1–26. [CrossRef]
9. Shao, Y.; Wyrwoll, K.-H.; Chappell, A.; Huang, J.; Lin, Z.; McTainsh, G.H.; Mikami, M.; Tanaka, T.Y.; Wang, X.; Yoon, S. Dust Cycle: An Emerging Core Theme in Earth System Science. *Aeolian Res.* **2011**, *2*, 181–204. [CrossRef]

10. Skonieczny, C.; McGee, D.; Winckler, G.; Bory, A.; Bradtmiller, L.I.; Kinsley, C.W.; Polissar, P.J.; Pol-Holz, R.D.; Rossignol, L.; Malaizé, B. Monsoon-Driven Saharan Dust Variability over the Past 240,000 Years. *Sci. Adv.* **2019**, *5*, eaav1887. [CrossRef]
11. Vandenbussche, S.; Callewaert, S.; Schepanski, K.; De Mazière, M. North African Mineral Dust Sources: New Insights from a Combined Analysis Based on 3D Dust Aerosol Distributions, Surface Winds and Ancillary Soil Parameters. *Atmos. Chem. Phys.* **2020**, *20*, 15127–15146. [CrossRef]
12. Prospero, J.M.; Ginoux, P.; Torres, O.; Nicholson, S.E.; Gill, T.E. Environmental Characterization of Global Sources of Atmospheric Soil Dust Identified with the Nimbus 7 Total Ozone Mapping Spectrometer (Toms) Absorbing Aerosol Product. *Rev. Geophys.* **2002**, *40*, 2-1–2-31. [CrossRef]
13. Scheuvens, D.; Schütz, L.; Kandler, K.; Ebert, M.; Weinbruch, S. Bulk Composition of Northern African Dust and Its Source Sediments—A Compilation. *Earth-Sci. Rev.* **2013**, *116*, 170–194. [CrossRef]
14. Gelado-Caballero, M.D. Saharan Dust Inputs to the Northeast Atlantic, Saharan Dust Inputs to the NE Atlantic, Oceanographic and Biological Features in the Canary Current Large Marine Ecosystem. In *Intergovernmental Oceanographic Commission; Technical Series: 115*; IOC-UNESCO: Paris, France, 2015; pp. 53–61.
15. von Suchodoletz, H.; Faust, D.; Zöller, L. Geomorphological Investigations of Sediment Traps on Lanzarote (Canary Islands) as a Key for the Interpretation of a Palaeoclimate Archive off NW Africa. *Quat. Int.* **2009**, *196*, 44–56. [CrossRef]
16. von Suchodoletz, H.; Fuchs, M.; Zöller, L. Dating Saharan Dust Deposits on Lanzarote (Canary Islands) by Luminescence Dating Techniques and Their Implication for Paleoclimate Construction of NW Africa. *Geochem. Geophys. Geosyst.* **2008**, *9*, Q02Q07. [CrossRef]
17. von Suchodoletz, H.; Kühn, P.; Hambach, U.; Dietze, M.; Zöller, L.; Faust, D. Loess-like and Palaeosol Sediments from Lanzarote (Canary Islands/Spain)—Indicators of Palaeoenvironmental Change during the Late Quaternary. *Palaeogeogr. Palaeoclimatol. Palaeoecol.* **2009**, *278*, 71–87. [CrossRef]
18. von Suchodoletz, H.; Oberhänsli, H.; Hambach, U.; Zöller, L.; Fuchs, M.; Faust, D. Soil Moisture Fluctuations Recorded in Saharan Dust Deposits on Lanzarote (Canary Islands) over the Last 180ka. *Quat. Sci. Rev.* **2010**, *29*, 2173–2184. [CrossRef]
19. von Suchodoletz, H.; Oberhänsli, H.; Faust, D.; Fuchs, M.; Blanchet, C.; Goldhammer, T.; Zöller, L. The Evolution of Saharan Dust Input on Lanzarote (Canary Islands)—Influenced by Human Activity in the Northwest Sahara during the Early Holocene? *Holocene* **2010**, *20*, 169–179. [CrossRef]
20. Carracedo, J.C.; Day, S.; Guillou, H.; Badiola, E.R.; Canas, J.A.; Torrado, F.J.P. Hotspot Volcanism Close to a Passive Continental Margin: The Canary Islands. *Geol. Mag.* **1998**, *135*, 591–604. [CrossRef]
21. Rothe, P. Kanarische Inseln/Lanzarote, Fuerteventura, Gran Canaria, Tenerife, Gomera, La Palma, Hierro; mit 9 Tabellen im Text und auf 5 Beilagen. In *Sammlung Geologischer Führer*; 81; Borntraeger: Berlin/Stuttgart, Germany, 1996; Volume 81, ISBN 978-3-443-15064-8.
22. Coello, J.; Cantagrel, J.-M.; Hernán, F.; Fúster, J.-M.; Ibarrola, E.; Ancochea, E.; Casquet, C.; Jamond, C.; Díaz de Téran, J.-R.; Cendrero, A. Evolution of the Eastern Volcanic Ridge of the Canary Islands Based on New K-Ar Data. *J. Volcanol. Geotherm. Res.* **1992**, *53*, 251–274. [CrossRef]
23. Gutiérrez-Elorza, M.; Lucha, P.; Gracia, F.-J.; Desir, G.; Marín, C.; Petit-Maire, N. Palaeoclimatic Considerations of Talus Flatirons and Aeolian Deposits in Northern Fuerteventura Volcanic Island (Canary Islands, Spain). *Geomorphology* **2013**, *197*, 1–9. [CrossRef]
24. Muhs, D.R.; Meco, J.; Budahn, J.R.; Skipp, G.L.; Simmons, K.R.; Baddock, M.C.; Betancort, J.F.; Lomoschitz, A. Long-Term African Dust Delivery to the Eastern Atlantic Ocean from the Sahara and Sahel Regions: Evidence from Quaternary Paleosols on the Canary Islands, Spain. *Quat. Sci. Rev.* **2021**, *265*, 107024. [CrossRef]
25. Menéndez, I.; Díaz-Hernández, J.L.; Mangas, J.; Alonso, I.; Sánchez-Soto, P.J. Airborne Dust Accumulation and Soil Development in the North-East Sector of Gran Canaria (Canary Islands, Spain). *J. Arid Environ.* **2007**, *71*, 57–81. [CrossRef]
26. Criado, C.; Dorta, P. An Unusual 'Blood Rain' over the Canary Islands (Spain). The Storm of January 1999. *J. Arid Environ.* **2003**, *55*, 765–783. [CrossRef]
27. Menéndez, I.; Pérez-Chacón, E.; Mangas, J.; Tauler, E.; Engelbrecht, J.P.; Derbyshire, E.; Cana, L.; Alonso, I. Dust Deposits on La Graciosa Island (Canary Islands, Spain): Texture, Mineralogy and a Case Study of Recent Dust Plume Transport. *CATENA* **2014**, *117*, 133–144. [CrossRef]
28. Mizota, C.; Matsuhisa, Y. Isotopic Evidence for the Eolian Origin of Quartz and Mica in Soils Developed on Volcanic Materials in the Canary Archipelago. *Geoderma* **1995**, *66*, 313–320. [CrossRef]
29. von Suchodoletz, H.; Zöller, L.; Hilgers, A.; Radtke, U.; Faust, D. Vegas and Dune Palaeosol-Sequences—Two Different Palaeoenvironmental Archives on the Eastern Canary Islands. In *Climate Change Perspectives from the Atlantic. Past, Present and Future*; Universidad de La Laguna de Tenerife: Tenerife, Spain, 2013; pp. 259–274, ISBN 978-84-15910-54-1.
30. Roettig, C.-B.; Varga, G.; Sauer, D.; Kolb, T.; Wolf, D.; Makowski, V.; Espejo, J.; Zöller, L.; Faust, D. Characteristics, Nature, and Formation of Palaeosurfaces within Dunes on Fuerteventura. *Quat. Res.* **2019**, *91*, 4–23. [CrossRef]

31. Schulte, P.; Lehmkuhl, F.; Steininger, F.; Loibl, D.; Lockot, G.; Protze, J.; Fischer, P.; Stauch, G. Influence of HCl Pretreatment and Organo-Mineral Complexes on Laser Diffraction Measurement of Loess–Paleosol-Sequences. *CATENA* **2016**, *137*, 392–405. [CrossRef]
32. Böttcher, J. Schlichting, J. Schlichting, E., Blume, H.-P. und Stahr, K.: Bodenkundliches Praktikum—Eine Einführung in pedologisches Arbeiten für Ökologen, insbesondere Land- und Forstwirte und für Geowissenschaftler. 2., neubearbeitete Auflage. Blackwell Wissenschafts-Verlag, Berlin, Wien, 1995; 295 S. Kartoniert, DM 58-, ISBN: 3-8263-3032-0. *Z. Für Pflanzenernährung Und Bodenkd.* **1995**, *159*, 313–314. [CrossRef]
33. Fuchs, M.; Fischer, M.; Reverman, R. Colluvial and Alluvial Sediment Archives Temporally Resolved by OSL Dating: Implications for Reconstructing Soil Erosion. *Quat. Geochronol.* **2010**, *5*, 269–273. [CrossRef]
34. Faust, D.; Yanes, Y.; Willkommen, T.; Roettig, C.; Richter, D.; Richter, D.; Suchodoletz, H.V.; Zöller, L. A Contribution to the Understanding of Late Pleistocene Dune Sand-Paleosol-Sequences in Fuerteventura (Canary Islands). *Geomorphology* **2015**, *246*, 290–304. [CrossRef]
35. Roettig, C.-B.; Kolb, T.; Wolf, D.; Baumgart, P.; Richter, C.; Schleicher, A.; Zöller, L.; Faust, D. Complexity of Quaternary Aeolian Dynamics (Canary Islands). *Palaeogeogr. Palaeoclimatol. Palaeoecol.* **2017**, *472*, 146–162. [CrossRef]
36. Murray, A.S.; Wintle, A.G. Luminescence Dating of Quartz Using an Improved Single-Aliquot Regenerative-Dose Protocol. *Radiat. Meas.* **2000**, *32*, 57–73. [CrossRef]
37. Murray, A.S.; Wintle, A.G. The Single Aliquot Regenerative Dose Protocol: Potential for Improvements in Reliability. *Radiat. Meas.* **2003**, *37*, 377–381. [CrossRef]
38. Galbraith, R.F.; Roberts, R.G.; Laslett, G.M.; Yoshida, H.; Olley, J.M. Optical Dating of Single and Multiple Grains of Quartz from Jinmium Rock Shelter, Northern Australia: Part I, Experimental Design and Statistical Models. *Archaeometry* **1999**, *41*, 339–364. [CrossRef]
39. Tudyka, K.; Bluszcz, A.; Poręba, G.; Miłosz, S.; Adamiec, G.; Kolarczyk, A.; Kolb, T.; Lomax, J.; Fuchs, M. Increased Dose Rate Precision in Combined α and β Counting in the µDose System—A Probabilistic Approach to Data Analysis. *Radiat. Meas.* **2020**, *134*, 106310. [CrossRef]
40. Kolb, T.; Tudyka, K.; Kadereit, A.; Lomax, J.; Poręba, G.; Zander, A.; Zipf, L.; Fuchs, M. The *µ*Dose System: Determination of Environmental Dose Rates by Combined Alpha and Beta Counting—Performance Tests and Practical Experiences. *Geochronology* **2022**, *4*, 1–31. [CrossRef]
41. Prescott, J.; Hutton, J. Cosmic Ray Contributions to Dose Rates for Luminescence and ESR Dating: Large Depths and Long-Term Time Variations. *Radiat. Meas.* **1994**, *23*, 497–500. [CrossRef]
42. Kreutzer, S.; Schmidt, C.; Fuchs, M.C.; Dietze, M.; Fischer, M.; Fuchs, M. Introducing an R Package for Luminescence Dating Analysis. *ATL* **2012**, *30*, 1–8. [CrossRef]
43. Durcan, J.A.; King, G.E.; Duller, G.A.T. DRAC: Dose Rate and Age Calculator for Trapped Charge Dating. *Quat. Geochronol.* **2015**, *28*, 54–61. [CrossRef]
44. Guérin, G.; Mercier, N.; Adamiec, G. Dose-Rate Conversion Factors: Update. *Ancient TL* **2011**, *29*, 5–8. [CrossRef]
45. Schneider, F.; Roettig, C.-B.; Wolf, D.; Baumgart, P.; Hambach, U.; Faust, D. Rock Magnetics of Carbonate Systems–Investigating Palaeodune Archives on Fuerteventura (Canary Islands). *J. Quat. Sci.* **2020**, *35*, 594–606. [CrossRef]
46. Song, Y.; Wei, H.; Xie, M.; Kang, S.; Zong, X.; Shukurov, N.; Shukurov, S.; Li, Y.; Li, Y.; Zhang, M. New Insights into Holocene Dust Activity in Eastern Uzbekistan. *Glob. Planet. Change* **2024**, *243*, 104633. [CrossRef]
47. Edwards, N.; Meco, J. Morphology and Palaeoenvironment of Brood Cells of Quaternary Ground-Nesting Solitary Bees (Hymenoptera, Apidae) from Fuerteventura, Canary Islands, Spain. *Proc. Geol. Assoc.* **2000**, *111*, 173–183. [CrossRef]
48. Durand, N.; Monger, H.C.; Canti, M.G.; Verrecchia, E.P. Chapter 9—Calcium Carbonate Features. In *Interpretation of Micromorphological Features of Soils and Regoliths*, 2nd ed.; Stoops, G., Marcelino, V., Mees, F., Eds.; Elsevier: Amsterdam, The Netherlands, 2018; pp. 205–258, ISBN 978-0-444-63522-8.
49. Alonso-Zarza, A.M.; Wright, V.P. Chapter 5 Calcretes. In *Developments in Sedimentology*; Alonso-Zarza, A.M., Tanner, L.H., Eds.; Carbonates in Continental Settings: Facies, Environments, and Processes; Elsevier: Amsterdam, The Netherlands, 2010; Volume 61, pp. 225–267.
50. Huerta Hurtado, P.; Rodríguez-Berriguete, Á.; Martín-García, R.; Martín-Pérez, A.; La Iglesia Fernández, Á.; Alonso-Zarza, A.M. The Role of Climate and Aeolian Dust Input in Calcrete Formation in Volcanic Islands (Lanzarote and Fuerteventura, Spain). *Palaeogeogr. Palaeoclimatol. Palaeoecol.* **2015**, *417*, 66–79. [CrossRef]
51. Zamanian, K.; Pustovoytov, K.; Kuzyakov, Y. Pedogenic Carbonates: Forms and Formation Processes. *Earth-Sci. Rev.* **2016**, *157*, 1–17. [CrossRef]
52. Littlewood, J.L.; Shaw, S.; Peacock, C.L.; Bots, P.; Trivedi, D.; Burke, I.T. Mechanism of Enhanced Strontium Uptake into Calcite via an Amorphous Calcium Carbonate Crystallization Pathway. *Cryst. Growth Des.* **2017**, *17*, 1214–1223. [CrossRef]
53. Rothwell, R.G.; Croudace, I.W. Twenty Years of XRF Core Scanning Marine Sediments: What Do Geochemical Proxies Tell Us? In *Micro-XRF Studies of Sediment Cores: Applications of a Non-Destructive Tool for the Environmental Sciences*; Croudace, I.W.,

Rothwell, R.G., Eds.; Developments in Paleoenvironmental Research; Springer: Dordrecht, The Netherlands, 2015; pp. 25–102, ISBN 978-94-017-9849-5.
54. Faure, G.; Bowman, J.R.; Elliot, D.H.; Jones, L.M. Strontium Isotope Composition and Petrogenesis of the Kirkpatrick Basalt, Queen Alexandra Range, Antarctica. *Contr. Mineral. Petrol.* **1974**, *48*, 153–169. [CrossRef]
55. Mc Kenzie, R.M. Manganese Oxides and Hydroxides. In *Minerals in Soil Environments*; John Wiley & Sons, Ltd.: Hoboken, NJ, USA, 1989; pp. 439–465, ISBN 978-0-89118-860-5.
56. Post, J.E. Manganese Oxide Minerals: Crystal Structures and Economic and Environmental Significance. *Proc. Natl. Acad. Sci. USA* **1999**, *96*, 3447–3454. [CrossRef]
57. Fiedler, S.; Sommer, M. Water and Redox Conditions in Wetland Soils—Their Influence on Pedogenic Oxides and Morphology. *Soil Sci. Soc. Am. J.* **2004**, *68*, 326–335. [CrossRef]
58. Fischel, M.; Clarke, C.; Sparks, D. Synchrotron Resolved Microscale and Bulk Mineralogy in Manganese-Rich Soils and Associated Pedogenic Concretions. *Geoderma* **2023**, *430*, 116305. [CrossRef]
59. Jahn, R. Böden Lanzarotes/Vorkommen, Genese u. Eigenschaften von Böden aus Vulkaniten im semiariden Klima Lanzarotes (Kanarische Inseln); 67 Tab. In *Hohenheimer Arbeiten*; Universität Hohenheim: Ulmer, Germany, 1988; ISBN 978-3-8001-8199-5.
60. Amelung, W.; Blume, H.-P.; Fleige, H.; Kandeler, E.; Kögel-Knabner, I.; Kretzschmar, R.; Stahr, K.; Wilke, B.-M. *Scheffer/Schachtschabel Lehrbuch Der Bodenkunde*; Springer: Berlin/Heidelberg, Germany, 2018; ISBN 978-3-662-55870-6.
61. Williamson, D.; Jackson, M.; Banerjee, S.K.; Petit-Maire, N. The Magnetism of a Glacial Aeolianite Sequence from Lanzarote (Canary Islands): Coupling between Luvic Calcisol Formation and Saharan Dust Trapping Processes during Wet Deposition Events off Northwestern Sahara. *Geophys. J. Int.* **2004**, *157*, 1090–1104. [CrossRef]
62. Cuadros, J.; Diaz-Hernandez, J.L.; Sanchez-Navas, A.; Garcia-Casco, A.; Yepes, J. Chemical and Textural Controls on the Formation of Sepiolite, Palygorskite and Dolomite in Volcanic Soils. *Geoderma* **2016**, *271*, 99–114. [CrossRef]
63. Thomas, D. *Arid Zone Geomorphology: Process, Form and Change in Drylands*; John Wiley & Sons: Hoboken, NJ, USA, 2011; Volume 116, ISBN 978-0-470-51908-0.
64. Goudie, A.S.; Wells, G.L. The Nature, Distribution and Formation of Pans in Arid Zones. *Earth-Sci. Rev.* **1995**, *38*, 1–69. [CrossRef]
65. Vainer, S.; Roskin, J.; Markin, M.; Raish, I.; Taha, N.; Porat, N.; Bookman, R. Sediments in Small Endorheic Basins as Regional Paleoenvironmental Archives across a Mediterranean to Arid Transect. *Quat. Sci. Rev.* **2025**, *367*, 109530. [CrossRef]
66. Jullien, E.; Grousset, F.; Malaizé, B.; Duprat, J.; Sanchez-Goni, M.F.; Eynaud, F.; Charlier, K.; Schneider, R.; Bory, A.; Bout, V.; et al. Low-Latitude "Dusty Events" vs. High-Latitude "Icy Heinrich Events". *Quat. Res.* **2007**, *68*, 379–386. [CrossRef]
67. Skonieczny, C.; Paillou, P.; Bory, A.; Bayon, G.; Biscara, L.; Crosta, X.; Eynaud, F.; Malaizé, B.; Revel, M.; Aleman, N.; et al. African Humid Periods Triggered the Reactivation of a Large River System in Western Sahara. *Nat. Commun.* **2015**, *6*, 8751. [CrossRef]
68. Moreno, A.; Targarona, J.; Henderiks, J.; Canals, M.; Freudenthal, T.; Meggers, H. Orbital Forcing of Dust Supply to the North Canary Basin over the Last 250kyr. *Quat. Sci. Rev.* **2001**, *20*, 1327–1339. [CrossRef]